Explicit Neural Network-derived formula for overtopping flow on mound breakwaters in depth-limited breaking wave conditions

Patricia Mares-Nasarre[1, *], Jorge Molines[1], M. Esther Gómez-Martín[1] and Josep R. Medina[1]

[1] Lab. Ports and Coasts, Institute of Transport and Territory, Universitat Politècnica de València; patmana@cam.upv.es, jormollo@upv.es, mgomar00@upv.es, jrmedina@upv.es.

* Corresponding author: patmana@cam.upv.es

Abstract:

Sea level rise due to climate change, as well as social pressure to decrease the visual impact of coastal structures, have led to reduced crest freeboards, and this increases the overtopping hazard. In previous studies, pedestrian safety during overtopping events was assessed considering the overtopping layer thickness (OLT) and the overtopping flow velocity (OFV). This study analyzed the statistics of OLT and OFV on mound breakwaters without crown walls during severe wave storms. Small-scale 2D physical tests were conducted on mound breakwaters with dimensionless crest freeboards between 0.29 and 1.77, testing three armor layers (single-layer Cubipod®, and double-layer cubes and rocks) in depth-limited breaking wave conditions and with two bottom slopes. Neural Networks were used to develop new estimators for the OLT and OFV exceeded by 2% of the incoming waves with a high coefficient of determination ($0.866 \leq R^2 \leq 0.876$). The best number of significant figures in the empirical coefficients of the new estimators was determined according to their variability. The 1-parameter Exponential and Rayleigh distribution functions were proposed to estimate the extreme values of OLT and OFV with $0.803 \leq R^2 \leq 0.812$, respectively.

Keywords: mound breakwater; wave overtopping; overtopping layer thickness; overtopping flow velocity; depth-limited breaking wave conditions; Cubipod®

1. Introduction

Coastal hazards are increasing due to the sea level rise and stronger wave storms caused by climate change (*Camus et al., 2019*). In addition, new social concerns demand decreasing visual and environmental impacts of infrastructures. The consequences of climate change and the satisfaction of new social demands influence coastal structure design; reduced design dimensionless crest freeboards and higher overtopping rates must be considered. Higher extreme overtopping events and overtopping risks are expected, leading to the need for new tools to better consider the current design conditions. In addition, most mound breakwaters are built in the surf zone in depth-limited breaking wave conditions.

During extreme wave overtopping events, overtopping water flows over the breakwater crest. The characteristics of such flow, overtopping layer thickness (OLT) and overtopping flow velocity (OFV), are directly related to the hydraulic stability of the breakwater crest and rear side (*Argente et al., 2018*), but also to pedestrian safety on the breakwater crest (*Bae et al., 2016*). Pedestrian safety becomes relevant as recreational activities such as fishing, walking or taking pictures often take place on the breakwater (see Figure 1).

Fig. 1. Pedestrians on mound breakwaters: (a) fishing in Scheveningen (the Netherlands) and (b) taking photos in Altea, (Spain).

There is extensive literature on the tolerable limits of water depth and flow velocity for pedestrian safety under constant flow conditions (*Abt et al.*, *1989*; *Endoh and Takahashi*, *1995*). Recently, *Bae et al.* (*2016)* and *Sandoval and Bruce* (*2017*) analyzed the stability of human bodies under overtopping flow conditions based on physical experiments with dummies and video images, respectively. *Bae et al.* (*2016*) also proposed tolerable limits for OLT and OFV for pedestrian accidents under overtopping flow conditions. Several predictors exist for OLT and OFV on dike crests (*Schüttrumpf and Van Gent*, *2003*; *van Bergeijk et al.*, *2019*). However, few studies are focused on OLT and OFV on mound breakwater crests (*Mares-Nasarre et al.*, *2020a*, *2019*). *Mares-Nasarre et al.* (*2020a*) demonstrated that the bottom slope (*m*) is a significant variable for estimating OLT and OFV, but *m* is not considered as an explanatory variable in the estimators found in the literature. Thus, methods given in the literature should be reviewed since none of the studies considered the bottom slope as an explanatory variable to estimate OLT and OFV.

This study examines the statistics of OLT and OFV on overtopped mound breakwaters (armor slope H/V = 3/2) without crown walls during extreme overtopping events under depth-limited breaking wave conditions and proposes new simple empirical formulas to estimate OLT and OFV exceeded by 2% of the incoming waves in the middle of the breakwater crest. In Section 2, the literature on OLT and OFV is analyzed, focusing on studies conducted on mound breakwaters. In Section 3, the experimental setup and data analysis are described; tests reported in *Mares-Nasarre et al.* (*2020a*) are used to fit the proposed empirical formulas and distribution functions. Small-scale models of mound breakwaters with single-layer randomly-placed Cubipod® (Cubipod®-1L), double-layer randomly-placed cube (cube-2L) and double-layer randomly-placed rock (rock-2L) armors were tested in the wave flume of the *Universitat Politècnica de València* (Spain) with two bottom slope configurations (*m* = 2% and 4%). Section 4 describes the Neural Network (NN) methodology used in this study to build up the empirical formulas with five explanatory variables for OLT and OFV. New estimators for OLT exceeded by 2% of the incoming waves as well as the statistical distribution function for the highest OLT (with exceedance probabilities under 2%) are described in Section 5. In Section 6, new estimators for OFV exceeded by 2% of the incoming waves and a statistical distribution function for OFV (with exceedance probabilities under 2%) are proposed. Finally, conclusions are drawn in Section 7.

2. Literature review on overtopping flow on mound breakwaters without crown wall

Few studies (*Mares-Nasarre et al.*, *2019*, *2020a*) can be found in the literature focused on OLT and OFV on mound breakwater crests. Thus, studies performed on sloping structures such as dikes are also reviewed in this section. It should be noted that dikes are sloping impermeable structures with smooth gentle slopes (seaward slope H/V > 3), whereas mound breakwaters are permeable structures (where infiltration occurs) with steeper slopes (seaward slope H/V ≤ 2).

Schüttrumpf et al. (*2002*) and *Van Gent* (*2002*) conducted the first studies analyzing OLT and OFV on dikes mainly in non-breaking conditions. *Schüttrumpf and Van Gent* (*2003*) combined their previous results and described the overtopping flow on a dike using two variables: (1) the OLT exceeded by 2% of the incoming waves ($h_{c2\%}$) and (2) the OFV exceeded by 2% of the incoming waves ($u_{c2\%}$). *Schüttrumpf and Van Gent* (*2003*) also proposed an empirical method to estimate $h_{c2\%}$ and $u_{c2\%}$ based on the wave run-up height exceeded by 2% of the incoming waves ($Ru_{2\%}$) calculated using the formulas in *Van Gent* (*2001*). *Van Gent* (*2001*) considered $Ru_{2\%}$ to be a function of the surf similarity parameter or Iribarren number ($Ir_{m-1,0}$) calculated with the significant wave height ($H_s = H_{1/3}$) and the spectral wave period $T_{m-1,0} = m_{-1}/m_0$, where m_i is the i-th spectral moment $m_i = \int_0^{\infty} S(f) f^i df$, being the wave spectrum $S(f)$. The main variables considered by *Schüttrumpf and Van Gent* (*2003*) are specified in Figure 2.

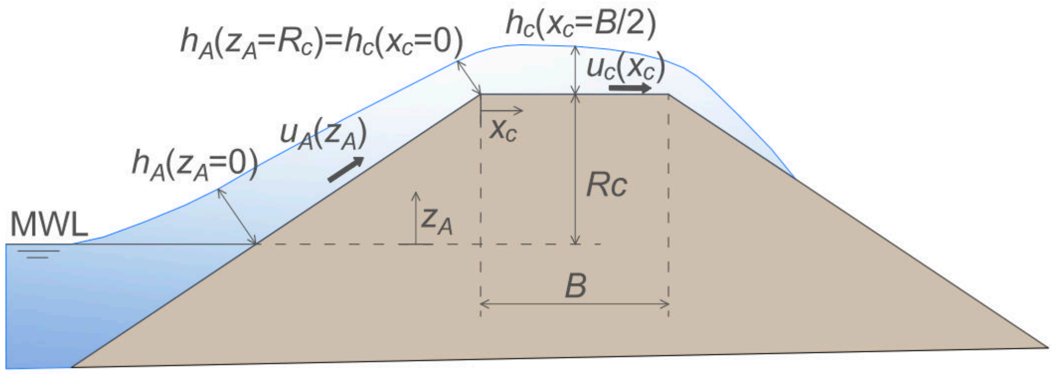

Fig. 2. Definition of the variables considered by Schüttrumpf and Van Gent (2003) *on a dike cross-section.*

According to *Schüttrumpf and Van Gent* (*2003*), OLT and OFV exceeded by 2% of the incoming waves at the seaward edge of the crest of the dike, $h_{A2\%}(z_A = R_c)$ and $u_{A2\%}(z_A = R_c)$, are estimated as

$$\frac{h_{A2\%}(z_A)}{H_s} = c^*_{A,h}\left(\frac{Ru_{2\%} - z_A}{H_s}\right) \tag{1}$$

$$\frac{u_{A2\%}(z_A)}{\sqrt{g\,H_s}} = c^*_{A,u}\sqrt{\frac{Ru_{2\%} - z_A}{H_s}} \tag{2}$$

where $c_{A,h}$* and $c_{A,u}$* are the empirical coefficients given in Table 1 and z_A is the elevation over the mean water level ($0 \le z_A \le R_c$). Once $h_{A2\%}(z_A = R_c)$ and $u_{A2\%}(z_A = R_c)$ are estimated using Eqs. (1) and (2), $h_{c2\%}$ and $u_{c2\%}$ can be calculated using Eqs. (3) and (4).

$$\frac{h_{c2\%}(x_c)}{h_{A2\%}(R_c)} = exp\left(-c^*_{c,h}\frac{x_c}{B}\right) \tag{3}$$

$$\frac{u_{c2\%}(x_c)}{u_{A2\%}(R_c)} = exp\left(-c^*_{c,u}\frac{x_c\,\mu}{h_{c2\%}(x_c)}\right) \tag{4}$$

where $c_{c,h}$* and $c_{c,u}$* are the empirical coefficients given in Table 1, x_c is the distance from the seaward side edge, B is the crest width and μ is the bottom friction coefficient. *Schüttrumpf et al.* (*2003*) proposed values of μ between 0.0058 and 0.02 for smooth slopes.

	Van Gent (2002)	*Schüttrumpf et al. (2002)*
R_c/H_{m0}	0.7 – 2.2	0.0 – 4.4
H_{m0}/h_s	0.2 – 1.4	0.1 – 0.3

Seaward slope ($\tan\alpha$=V/H)	1/4	1/3, 1/4, 1/6
$c_{A,h}$*	0.15	0.33
c_{A,u^*}	1.30	1.37
$c_{c,h}$*	0.40	0.89
c_{c,u^*}	0.50	0.50

Table 1. Experimental ranges and empirical coefficients for Eqs. (1) to (4).

Therefore, $h_{c2\%}$ and $u_{c2\%}$ estimated using the methods described in *Schüttrumpf and Van Gent* (*2003*) depend on H_s and $T_{m-1,0}$ as well as the seaward slope, $\tan\alpha$, the crest freeboard, R_c, and the crest width of the dike, B.

Van der Meer et al. (*2010*) considered the same variables as *Schüttrumpf and Van Gent* (*2003*) to explain $h_{c2\%}$ when analyzing new tests in the overtopping simulator. Regarding $u_{c2\%}$, *Van der Meer et al.* (*2010*) included $L_{m-1,0}$, the wavelength based on $T_{m-1,0}$. *Lorke et al.* (*2012*) and *Formentin et al.* (*2019*) proposed new formulas to estimate $h_{c2\%}$ and $u_{c2\%}$ on dikes with no additional explanatory variables.

Mares-Nasarre et al. (*2019*) was the first study focusing on OLT and OFV on overtopped mound breakwaters (armor slope H/V = 3/2); the experimental range of the dimensionless crest freeboard was $0.34 \le R_c/H_{m0} \le 1.75$, where $H_{m0} = 4(m_0)^{0.5}$ is the spectral significant wave height, and three armor layers (Cubipod®-1L, cube-2L and rock-2L) were tested under depth-limited breaking wave conditions ($0.20 \le H_{m0}/h_s \le 0.73$, where h_s is the water depth at the toe of the structure). *Mares-Nasarre et al.* (*2019*) performed tests with a bottom slope m = 2% and measured OLT and OFV in the middle of the breakwater crest. These researchers adapted Eqs. (1) and (3) proposed by *Schüttrumpf and Van Gent* (*2003*) to estimate $h_{c2\%}$ in the middle of the breakwater crest, $h_{c2\%}(B/2)$. Since the formulas given by *Schüttrumpf and Van Gent* (*2003*) are based on $Ru_{2\%}$, *Mares-Nasarre et al.* (*2019*) recommended Eq. (5) given by *EurOtop* (*2018*) to estimate $Ru_{2\%}$.

$$\frac{Ru_{2\%}}{H_s} = 1.65\,\gamma_f\,\gamma_\beta\,\gamma_b\,Ir_{m-1,0} \tag{5a}$$

with a maximum value of

$$\frac{Ru_{2\%}}{H_s} = 1.00\,\gamma_{f,surging}\gamma_\beta\,\gamma_b\left(4.0 - \frac{1.5}{\sqrt{Ir_{m-1,0}}}\right) \tag{5b}$$

where γ_f is the roughness coefficient depending on the type of armor, γ_β is the factor which takes into account the effect of oblique wave attack, γ_b is the influence factor for berms and $\gamma_{f,surging}$ [-] is the roughness coefficient that increases linearly up to 1.0 following

$$\gamma_{f,surging} = \gamma_f + \left(Ir_{m-1,0} - 1.8\right)\frac{1-\gamma_f}{8{,}2} \tag{5c}$$

The maximum $Ru_{2\%}/H_s$ is 2.0 for permeable core. In *Mares-Nasarre et al.* (*2019*), $\gamma_\beta = \gamma_b = 1$.

Mares-Nasarre et al. (*2019*) calibrated $c_{A,h}$*, $c_{c,h}$* and γ_f following the recommendations by *Molines and Medina* (*2015*) and proposed $c_{A,h}$* = 0.52, $c_{c,h}$* = 0.89 and γ_f = 0.33, 0.35 and 0.48 for Cubipod®-1L, cube-2L and rock-2L, respectively, in Eqs. (1) and (3). *Mares-Nasarre et al.* (*2019*) calculated $u_{c2\%}$ in the middle of the breakwater crest, $u_{c2\%}(B/2)$, as function of the squared root of $h_{c2\%}(B/2)$; $u_{c2\%}(B/2) = K_2\,(g h_{c2\%}(B/2))^{0.5}$, where K_2 was calibrated for each armor layer. K_2 = 0.57, 0.60 and 0.47 were proposed for

Cubipod®-1L, cube-2L and rock-2L, respectively. These authors also described the highest values of OLT and OFV in the middle of the breakwater crest using the 1-parameter Exponential and Rayleigh distributions.

Mares-Nasarre et al. (*2020a*) recently expanded the database used in *Mares-Nasarre et al.* (*2019*) conducting 2D physical tests with m = 4%. Similar to *Mares-Nasarre et al.* (*2019*), overtopped mound breakwaters were tested with the same three armor layers (Cubipod®-1L, cube-2L and rock-2L) under depth-limited breaking wave conditions ($0.20 \leq H_{m0}/h_s \leq 0.90$). As pointed out by *Herrera et al.* (*2017*), in depth-limited breaking wave conditions, the optimum point to estimate the incident wave characteristics is relevant. Thus, *Mares-Nasarre et al.* (*2020a*) analyzed the optimum point to estimate wave characteristics in order to calculate $h_{c2\%}(B/2)$ and $u_{c2\%}(B/2)$; the optimum point was found at a distance of $3h_s$ from the toe of the structure. This distance was also recommended by *Herrera et al.* (*2017*) and approximately corresponds to $5H_s$ suggested by *Goda* (*1985)* and *Melby* (*1999*). It was found that $h_{c2\%}(B/2)$ decreased while $u_{c2\%}(B/2)$ slightly increased for increasing values of m; therefore, m is a significant variable to consider when estimating $h_{c2\%}(B/2)$ and $u_{c2\%}(B/2)$ on mound breakwater crests.

3. Experimental methodology

3.1. Experimental setup

Mares-Nasarre et al. (*2019* and *2020a*) carried out 2D physical tests in the wave flume (30 m × 1.2 m × 1.2 m) of the Laboratory of Ports and Coasts at the *Universitat Politècnica de València* (LPC-UPV), with two mild bottom slope configurations. The first configuration was composed of two ramps: one 6.25 m-long m = 4% bottom slope, and another 9.0 m-long m = 2% bottom slope. The second configuration consisted of a continuous ramp of m = 4% all along the wave flume. Figure 3 shows the longitudinal cross-sections of the LPC-UPV wave flume for the two configurations with the locations of the wave gauges.

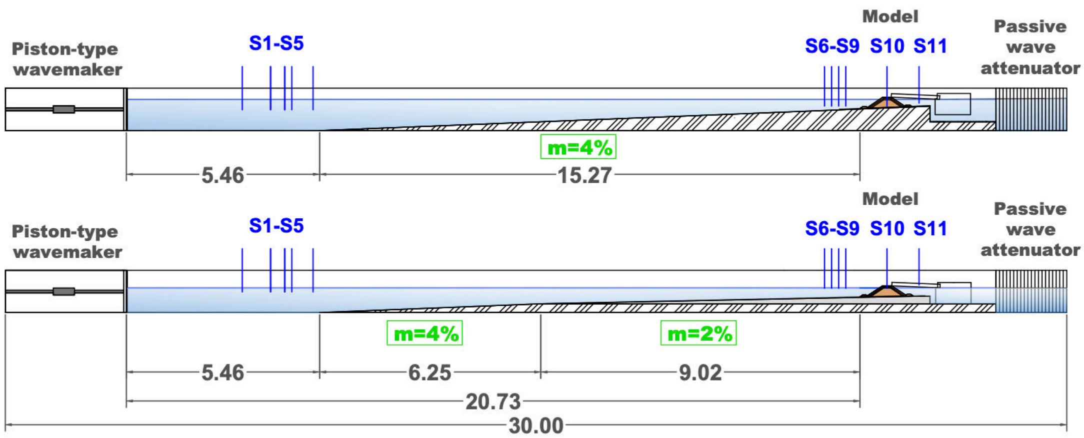

Fig. 3. Longitudinal cross-sections of the LPC-UPV wave flume.

11 capacitive wave gauges were placed along the flume to measure the water surface elevation. Wave gauges S1 to S5 were installed in the wave generation zone following the recommendations by *Mansard and Funke* (*1980*) in order to separate incident and reflected waves in the wave generation zone. Wave gauges S6 to S9 were located close to the model. Note that close to the model, depth-limited wave breaking occurs, and the existing methods to separate incident and reflected waves are not reliable. The distances from S6, S7, S8 and S9 to the model toe were $5h_s$, $4h_s$, $3h_s$ and $2h_s$, respectively. Wave gauge S10 was placed in the middle of the breakwater crest in order to analyze OLT, while S11 was installed behind the model to detect possible phenomena of water piling-up.

Irregular wave tests with 1,000 waves were generated following a JONSWAP spectrum (γ = 3.3). The AWACS wave absorption system was activated during the tests to avoid multireflections. Neither low-frequency oscillations nor piling-up (S11) were significant during the tests. Piling-up is an undesirable phenomenon which consists of an increase in the water depth behind the model due to the accumulation of water caused by high overtopping rates and other effects. The LPC-UPV wave flume prevents piling-up by allowing the water to recirculate through a double floor.

The tested cross-section depicted in Figure 4 corresponds to a mound breakwater with armor slope H/V = 3/2 and rock toe berms. Three armor layers were tested: single-layer Cubipod® (Cubipod®-1L with nominal median diameter or equivalent cube size D_{n50}= 3.79 cm), double-layer randomly-placed cube (cube-2L with D_{n50} = 3.97 cm) and double-layer randomly-placed rock (rock-2L with D_{n50} = 3.18 cm) armors. Tests conducted with m = 2% were performed with a medium-sized rock toe berm (D_{n50} = 2.6 cm) while tests carried out with m = 4% were conducted with a larger rock toe berm (D_{n50} = 3.9 cm) in order to guarantee the toe berm hydraulic stability during the tests.

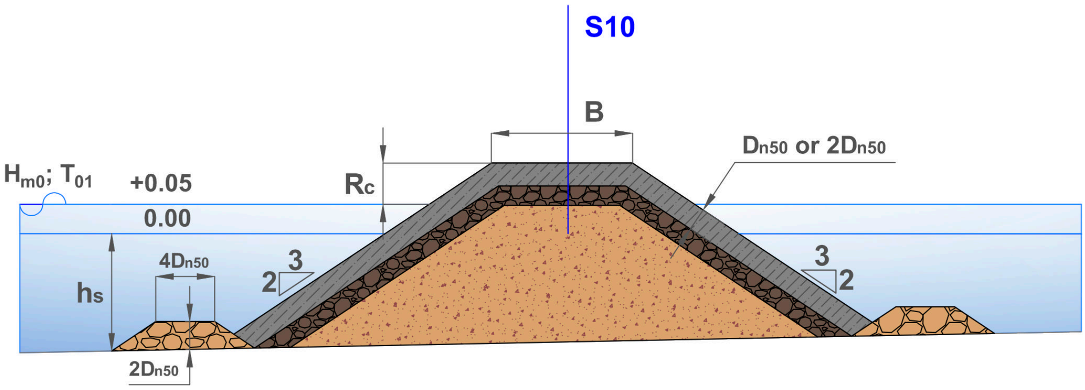

Fig. 4. Cross-section of the models tested in the LPC-UPV wave flume. Dimensions in m.

Each breakwater model was built on bottom flume configurations m = 2% and 4% and two water depths (h_s) at the toe of the structure were considered. h_s = 20 cm and 25 cm were tested for all the cases except the test series corresponding to cube-2L with m = 2%; in these specific case test series, h_s = 25 cm and 30 cm were tested. For each water depth (h_s), H_{m0} and peak period (T_p) were calculated at the wave generation zone, in order to keep the wave steepness ($s_{0p} = H_{m0}/L_{0p} = 2\pi H_{m0}/(gT_p^2)$) approximately constant through each test series (s_{0p} = 0.02 and 0.05). For each s_{0p}, H_{m0} at the wave generation zone ($H_{m0,g}$) was increased in steps of 1 cm from no damage to initiation of damage of the armor layer or wave breaking at the wave generation zone. Table 2 shows the range of the main variables considered during the tests. Note that wave characteristics (H_{m0} and $T_{m-1,0}$) are provided at a distance of 3h_s from the toe of the structure following recommendations by *Mares-Nasarre et al. (2020a)*.

m	Armor	B [m]	#tests	h_s [m]	R_c [m]	H_{m0} [m]	$T_{m-1,0}$ [s]
1/50	Cubipod® - 1L	0.24	25	0.20	0.12	0.08 – 0.15	1.04 – 1.98
			28	0.25	0.07	0.07 – 0.17	0.93 – 2.04
	cube – 2L	0.27	26	0.25	0.11	0.07 – 0.16	0.95 – 2.05
			23	0.30	0.06	0.07 – 0.18	0.89 – 1.89
	rock – 2L	0.26	8	0.20	0.15	0.09 – 0.13	1.12 – 1.70
			13	0.25	0.10	0.07 – 0.13	0.89 – 1.73
1/25	Cubipod® - 1L	0.24	21	0.20	0.12	0.09 – 0.17	1.04 – 1.88
			28	0.25	0.07	0.07 – 0.18	0.94 – 2.15
	cube – 2L	0.27	21	0.20	0.11	0.10 – 0.17	1.14 – 1.87

			23	0.25	0.06	0.09 – 0.18	1.06 – 2.15
	rock – 2L	0.26	8	0.20	0.15	0.10 – 0.14	1.25 – 1.89
			11	0.25	0.10	0.09 – 0.14	1.08 – 1.91

Table 2. Structural and wave characteristics of the 2D tests corresponding to single (1L) and double-layer (2L) armors.

Three cameras were also installed in order to analyze the armor damage in the frontal slope, crest and rear side of the armor using the Virtual Net Method (*Gómez-Martín and Medina, 2014*). Overtopping discharges were collected using a chute and a weighing system placed in a collection tank behind the model (*Mares-Nasarre et al., 2020b*).

3.2. Wave analysis

Waves in the wave generation zone were separated using the measurements taken by wave gauges S1 to S5 and the LASA-V method (*Figueres and Medina, 2005*). The LASA-V method is applicable to nonstationary and nonlinear irregular waves. However, the existing methods given in the literature are not valid for breaking waves. Thus, to estimate incident waves in the model zone, where wave breaking occurs, the SwanOne propagation model (*Verhagen et al., 2008*) was used. The SwanOne model fits a JONSWAP spectrum (γ=3.3) based on the input incident wave conditions in the wave generation zone. This spectrum is propagated along the bathymetry of the wave flume and the Composite Weibull distribution recommended by *Battjes and Groenendijk* (*2000*) is applied to describe the wave height distribution in shallow foreshores. Note that the SwanOne model analyzes frequencies within the range 0.03 – 0.8 Hz, since it is prepared for prototype scale wave conditions; in this study, a reference scale 1/30 was assumed.

Herrera and Medina (*2015*) validated the SwanOne model using tests without a structure. In the present study, a similar validation was conducted; tests without a structure were performed using an efficient passive wave absorption system at the end of the flume ($K_r = H_{m0,r}/H_{m0,i} < 0.25$). The measurements of the tests without a structure (total waves) were compared with the SwanOne model simulations at both the wave generation zone (Figure 5a and 5c) and the model zone (Figure 5b and 5d). Note that SwanOne simulations at the wave generation zone represent the fitting to the input incident waves obtained after separating incident and reflected waves using measurements taken by wave gauges S1 to S5.

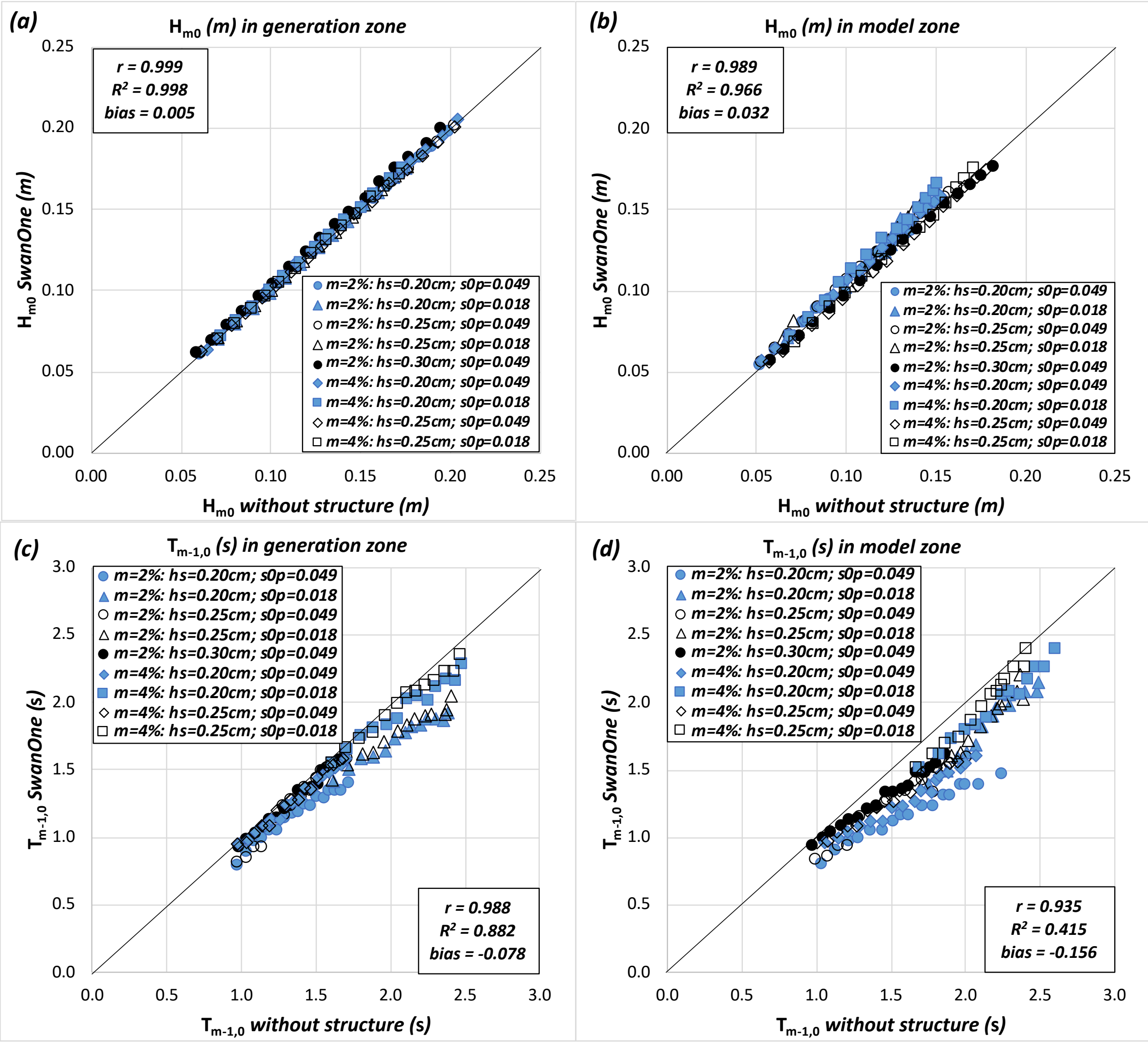

Fig. 5. Comparison between the measured wave characteristics in the tests without a structure and the estimations for incident waves given by the SwanOne model for: (a) significant wave height in the generation zone, (b) significant wave height in the model zone, (c) spectral period $T_{m-1,0}$ *in the generation zone and (d) spectral period* $T_{m-1,0}$ *in the model zone.*

Correlation coefficient (*r*), coefficient of determination (R^2) and relative bias (*bias*) were considered to quantify the goodness of fit in this study. $0 \leq r \leq 1$ assesses the correlation, $0 \leq R^2 \leq 1$ estimates the proportion of variance explained by the model and $-1 \leq bias \leq 1$ provides a dimensionless quantification of the bias. Thus, the higher the *r*, the higher the R^2 and the closer the *bias* to 0, the better.

$$r = \frac{\sum_{i=1}^{N_{ob}}(o_i - \bar{o})(e_i - \bar{e})}{\sqrt{\sum_{i=1}^{N_{ob}}(o_i - \bar{o})^2 \sum_{i=1}^{N_o}(e_i - \bar{e})^2}} \tag{6}$$

$$R^2 = 1 - \frac{\frac{1}{N_{ob}} \sum_{i=1}^{N_o}(o_i - e_i)^2}{\frac{1}{N_{ob}} \sum_{i=1}^{N_o}(o_i - \bar{o})^2} \tag{7}$$

$$bias = \frac{1}{N_{ob}} \sum_{i=1}^{N_{ob}} \frac{(e_i - o_i)}{|o_i|} \tag{8}$$

where N_{ob} is the number of observations, o_i and e_i are the observed and estimated values, and $\bar{o}$ is the average observed value. As shown in Figure 5, agreement was reasonable for the fitted conditions in the wave generation zone ($R^2 \geq 0.882$). Regarding the model zone, good agreement was observed for H_{m0} ($R^2 = 0.966$) while poor results were obtained for $T_{m-1,0}$ ($R^2 = 0.415$). As reported in *Mares-Nasarre et al.* (*2020b*), decreasing values of *bias* were observed for H_{m0} in the model zone for increasing values of h_s.

During the design phase of a mound breakwater, the design wave conditions (H_{m0} and $T_{m-1,0}$) must be estimated at the location where the mound breakwater will be built; thus, both H_{m0} and $T_{m-1,0}$ estimated by SwanOne are applied in this study.

3.3. Overtopping layer thickness (OLT) and Overtopping flow velocity (OFV) measurement

OLT was recorded in 57 physical tests, while OLT and OFV were measured in an additional 178 physical tests. OLT was measured using a capacitive wave gauge (S10) located in the middle of the breakwater crest (see Figures 3 and 4). S10 was inserted into a hollow cylinder filled with water in order to keep the sensor partially submerged. A lid with a slot was installed in the upper part of the cylinder to prevent water loss and to maintain the daily-calibrated reference level. The cylinder was 12 cm in length and 8.5 cm in diameter. Visual inspection of the OLT during overtopping events showed a clear water surface (see Figure 6). Thus, aeration was considered negligible. Little variation in the reference level was seen and little noise was measured, as shown in Figure 7.

Fig. 6. Visual inspection of the overtopping layer thickness (OLT) during the physical tests.

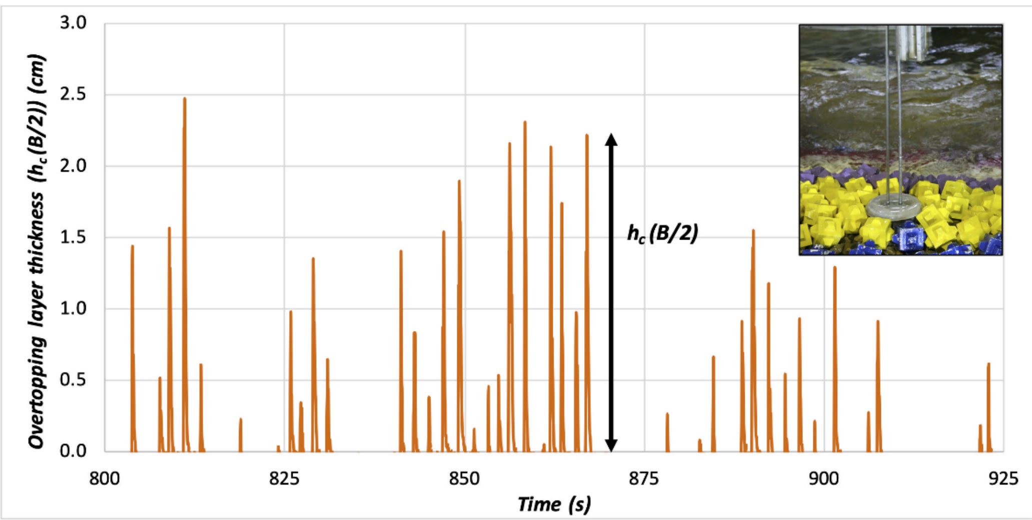

Fig. 7. Example of a raw record taken by wave gauge S10.

The OFV was measured at a frequency of 20 Hz using three miniature propellers installed along the crest: (1) on the seaward edge of the model crest, (2) in the middle of the model crest, and (3) on the leeward edge of the model crest. In this study, the measurements taken in the middle of the breakwater crest were used. The operational range of these miniature propellers was $0.15 < u(\mathrm{m/s}) < 3.00$. Thus, OFV values below 0.15 m/s were disregarded. Figure 8 displays an example of a record from a miniature propeller.

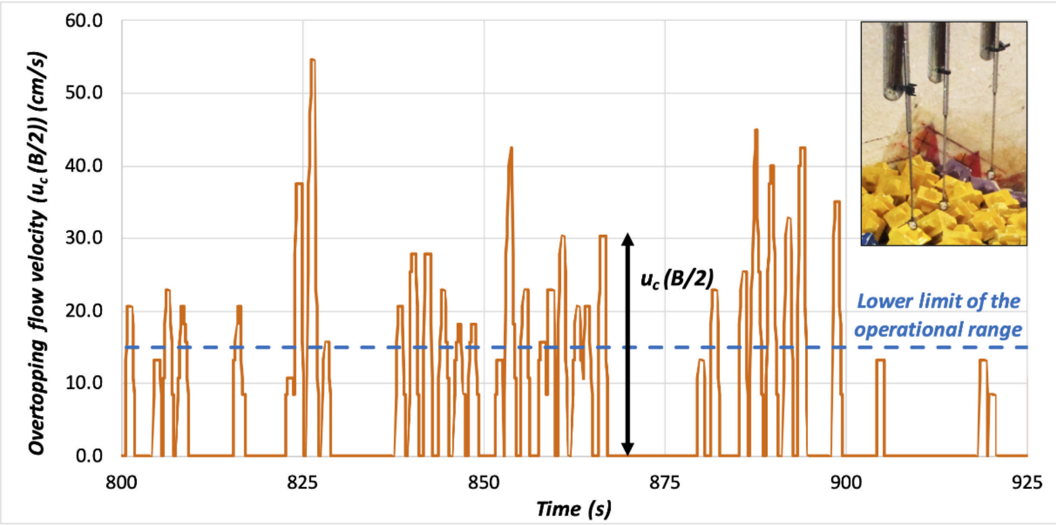

Fig. 8. Example of a raw record of a miniature propeller.

4. Methodology of analysis using Neural Networks (NNs)

Feedforward Neural Network (NN) models are commonly used in the artificial intelligence field to model nonlinear relationships between explanatory variables (input) and response variables (output). During the last two decades, NN models have been applied successfully by researchers and practitioners to estimate wave overtopping, wave reflection or wave forces on coastal structures. NN models have also been used in practical applications with a large database of wave overtopping tests (*van Gent et al., 2007; Formentin et al., 2017*) and with smaller datasets to identify the most relevant variables to estimate wave forces on crown walls (*Molines et al., 2018*), or to define explicit wave overtopping formulae (*Molines and Medina, 2016*). In this research, Multi-layer feedforward NN models were used to analyze the influence of a set of explanatory variables on $h_{c2\%}(B/2)$ and $u_{c2\%}(B/2)$.

4.1. Explanatory variables affecting $h_{c2\%}(B/2)$ and $u_{c2\%}(B/2)$

Based on the literature, the explanatory variables which might influence $h_{c2\%}(B/2)$ and $u_{c2\%}(B/2)$ are m, R_c, H_{m0}, $T_{m-1,0}$ and h_s (with H_{m0} and $T_{m-1,0}$ located at a distance of $3h_s$ from the toe of the structure). These explanatory variables consider the wave conditions at the toe of the structure and the crest freeboard. In order to ensure a NN model is not affected by the model scale, the aforementioned explanatory variables were made dimensionless as:

- R_c/H_{m0}, is the dimensionless crest freeboard and is the most common and widely accepted dimensionless variable that governs the mean wave overtopping discharge.
- $Ir_{m-1,0}=\tan\alpha/(H_{m0}/L_{m-1,0})^{0.5}$, is the Iribarren number or breaker parameter calculated using H_{m0} and $T_{m-1,0}$ at a distance of $3h_s$ from the toe of the structure. $Ir_{-m1,0}$ considers the influence of the wave steepness and armor slope and determines the type of wave breaking on the slope. In this study, only $\tan\alpha=2/3$ was tested; however, $Ir_{m-1,0}$ was selected instead of wave steepness, since *Schüttrumpf and Van Gent* (*2003*) reported $Ir_{m-1,0}$ as significant. The influence of $Ir_{-m1,0}$ on wave overtopping was also reported in studies such as *Molines and Medina* (*2016*).

- m, is the bottom slope, which determines the type of wave breaking on the toe of the structure. *Mares-Nasarre et al.* (*2020a*) determined that m plays a significant role in the estimation of OLT and OFV.

- h_s/H_{m0}, is the dimensionless water depth using the water depth at the toe of the structure and H_{m0} at a distance of $3h_s$ from the toe of the structure. h_s/H_{m0} is commonly used as a breaking index to indicate if waves are depth-limited or not (*Nørgaard et al., 2014*; *van Gent, 1999*).

Both $h_{c2\%}(B/2)$ and $u_{c2\%}(B/2)$ were also analyzed as dimensionless variables: $h_{c2\%}(B/2)/H_{m0}$ and $u_{c2\%}(B/2)/(H_{m0}/T_{m-1,0})$.

4.2. General outline

For each type of armor (Cubipod®-1L, cube-2L and rock-2L), a NN model was trained to estimate $h_{c2\%}(B/2)$ and $u_{c2\%}(B/2)$ independently. Thus, six NN models were developed (3 types of armors x 2 output variables).

For each NN model, the dataset (*N* cases) was randomly divided in two parts: *TR*=75%x*N* to develop the NN model and *T*=25%x*N* for a final blind test (*T-BLIND*) in which the NN model performance was evaluated with data not used to develop the NN model. The NN models connected neurons using a hyperbolic tangent sigmoid transfer function; the NN models presented an input layer with 4 neurons (N_i), a hidden layer with 3 neurons (N_h) and an output layer with 1 neuron (N_o), see Figure 9. Thus, the number of free parameters in the NN model is given by $P = N_o + N_h\ (N_i + N_o + 1) = 19$.

In this study, $P/TR < 0.63$ and the Early Stopping Criterion were applied to prevent overlearning (see *The MathWorks Inc., 2019*). The Early Stopping Criterion randomly divides the dataset *TR* in three categories: (1) training of the NN (70% × *TR*=*TRAIN*), (2) validation (15% × *TR*=*VAL*) and (3) testing (15% × *TR*=*TEST*). Data in the training subset were used to update the biases and weights of the NN. Data in the validation subset were used to monitor the error after each training step and to stop the training process once the error in this validation subset started growing (indicating possible overlearning). Data in the testing subset were used as cross validation to compare different models, since they were not included in the training process.

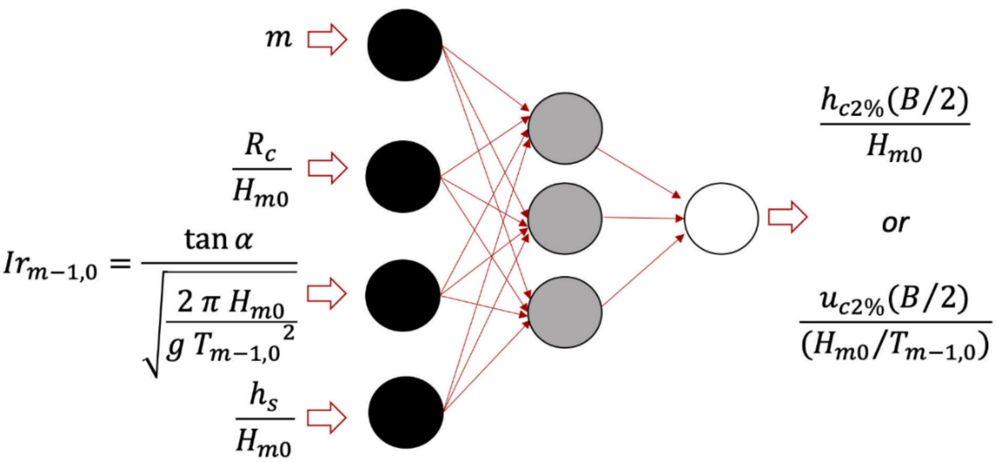

Fig. 9. Architecture of the Neural Network models used in this study.

4.3. NN model results

Figures 10a and 10b illustrate the performance of the NN models for $h_{c2\%}(B/2)/H_{m0}$ and $u_{c2\%}(B/2)/(H_{m0}/T_{m-1,0})$ using the training (*TRAIN*), validation (*VAL*) and testing (*TEST*) subset. A good performance was observed in the testing subset with R^2 = 0.903 and 0.789 for $h_{c2\%}(B/2)/H_{m0}$ and $u_{c2\%}(B/2)/(H_{m0}/T_{m-1,0})$, respectively. Figures 10c and 10d compare the measured and estimated

$h_{c2\%}(B/2)/H_{m0}$ and $u_{c2\%}(B/2)/(H_{m0}/T_{m-1,0})$ using the NN models on the 25% experimental data reserved for the final blind test (*T-BLIND*). A good agreement was found with $R^2 = 0.913$ for $h_{c2\%}(B/2)/H_{m0}$ and $R^2 = 0.918$ for $u_{c2\%}(B/2)/(H_{m0}/T_{m-1,0})$. Note that $R^2 = 0.164$ was obtained when assessing the goodness-of-fit of the NN developed for $u_{c2\%}(B/2)/(H_{m0}/T_{-1,0})$ on Cubipod®-1L using the *TEST* subset due to the low variance of the randomly selected testing subset (variance of the *TEST* subset was 0.15 while the variance of the whole *TR* dataset was 0.90).

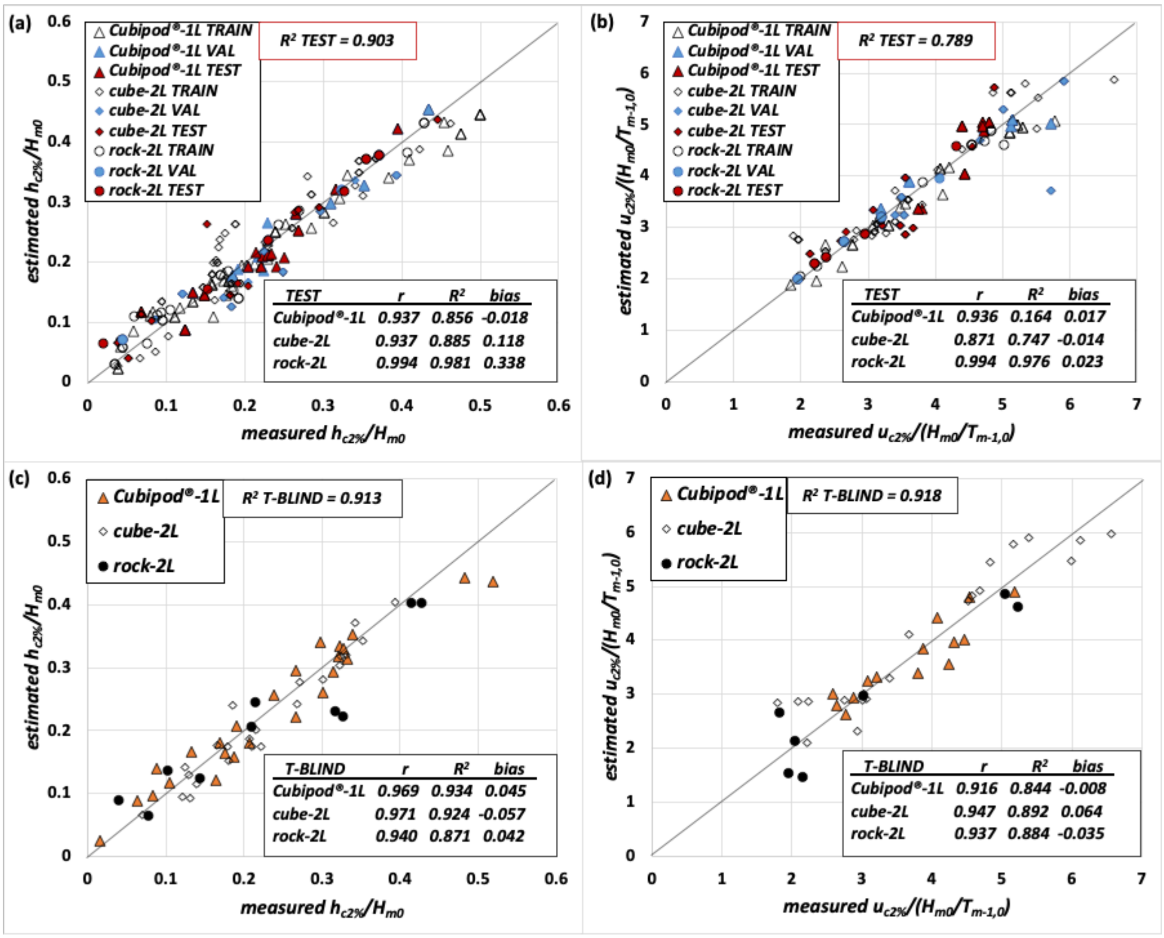

Fig. 10. Comparison between measured and estimated OLT and OFV with the NN models: (a) $h_{c2\%}(B/2)/H_{m0}$ *on the testing subset (TEST), (b)* $u_{c2\%}(B/2)/(H_{m0}/T_{m-1,0})$ *on the testing subset (TEST), (c)* $h_{c2\%}(B/2)/H_{m0}$ *on the final blind test subset (T-BLIND) and (d)* $u_{c2\%}(B/2)/(H_{m0}/T_{m-1,0})$ *on the final blind test subset (T-BLIND).*

4.4. Influence of the explanatory variables on $h_{c2\%}(B/2)/H_{m0}$ *and* $u_{c2\%}(B/2)/(H_{m0}/T_{m-1,0})$

NN models trained in Sections 4.1 to 4.3 were used here to analyze the influence of the four explanatory dimensionless variables (m, R_c/H_{m0}, $Ir_{m-1,0}$ and h_s/H_{m0}) on $h_{c2\%}(B/2)/H_{m0}$ and $u_{c2\%}(B/2)/(H_{m0}/T_{m-1,0})$. To this end, simulations were performed with variations in only one input variable while keeping the value of the other input variables constant. Figure 11 illustrates the influence of R_c/H_{m0} on $h_{c2\%}(B/2)/H_{m0}$. Figure 11a shows the simulations performed using the NN model for Cubipod®-1L armor corresponding to the inputs m = 4%, $Ir_{m-1,0}$ = 3.5, 4.0 and 4.5, and h_s/H_{m0} = 2.0. Figure 11b shows the differences between NN simulations corresponding to Cubipod®-1L, cube-2L and rock-2L armors for m = 4%, $Ir_{m-1,0}$ = 4.0 and h_s/H_{m0} = 2.0. Figure 11 shows that a linear model is suitable to describe the influence of R_c/H_{m0} on $h_{c2\%}(B/2)/H_{m0}$. Similar figures were obtained to describe the influence of m, R_c/H_{m0} and h_s/H_{m0} on $h_{c2\%}(B/2)/H_{m0}$; thus, a linear model was found to be suitable to describe the influence of the four dimensionless input variables on $h_{c2\%}(B/2)/H_{m0}$. Note that only linear relationships between m and the studied variables, namely $h_{c2\%}(B/2)/H_{m0}$ and $u_{c2\%}(B/2)/(H_{m0}/T_{m-1,0})$, were reasonable, since only two values of m were tested in this study, and the model is only valid in the range $2\% \le m \le 4\%$.

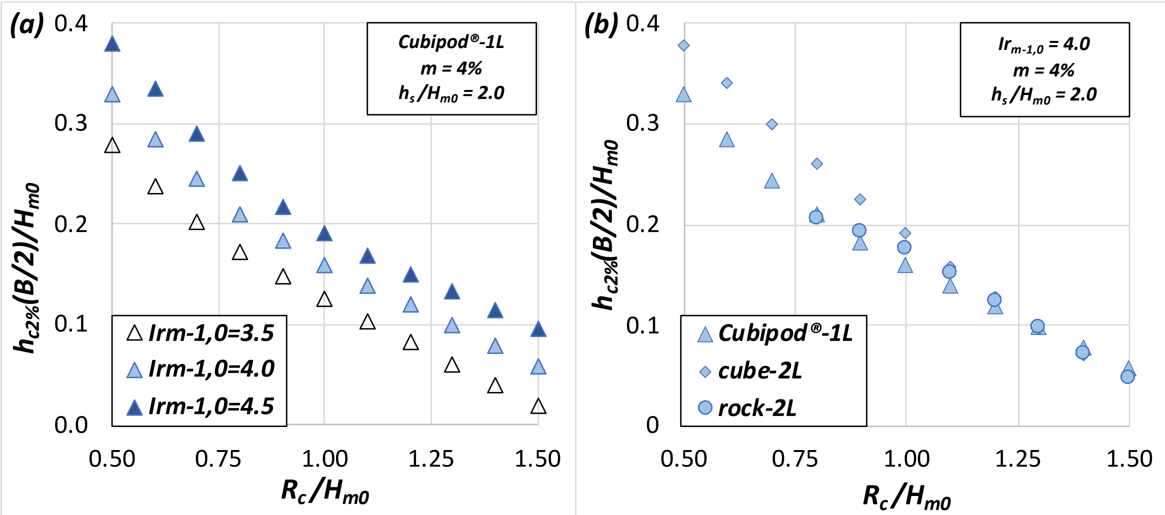

Fig. 11. Influence of R_c/H_{m0} *on* $h_{c2\%}(B/2)/H_{m0}$ *with* m=4%, h_s/H_{m0}=2.0 *and constant* $Ir_{m-1,0}$.

Figure 12a shows the NN simulations conducted for cube-2L with m = 2%, R_c/H_{m0} = 0.5, 1.0 and 1.5 and h_s/H_{m0} = 2.5. Figure 12b illustrates the differences between NN simulations corresponding to Cubipod®-1L, cube-2L and rock-2L armors for m = 2%, R_c/H_{m0} = 1.5 and h_s/H_{m0} = 2.5. Figure 12 illustrates that the influence of $Ir_{m-1,0}$ on $u_{c2\%}(B/2)/(H_{m0}/T_{m-1,0})$ followed a quadratic relationship. On the other hand, a linear relationship was observed between m, R_c/H_{m0} and h_s/H_{m0} and $u_{c2\%}(B/2)/(H_{m0}/T_{m-1,0})$.

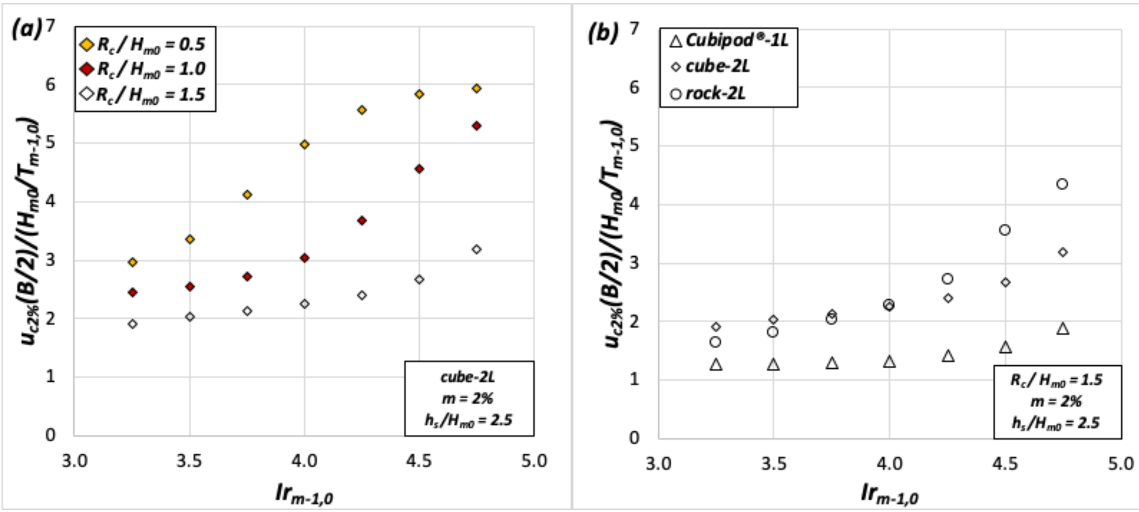

Fig. 12. Influence of $Ir_{m-1,0}$ *on* $u_{c2\%}(B/2)/(H_{m0}/T_{m-1,0})$ *with* m=2%, h_s/H_{m0}=2.5 *and constant* R_c/H_{m0}.

5. Estimating overtopping layer thickness (OLT) on mound breakwaters

5.1. Overtopping layer thickness (OLT) exceeded by 2% of the incoming waves

In Section 4.4, the simulations conducted with NN models were used to analyze the influence of the explanatory variables on $h_{c2\%}(B/2)/H_{m0}$. Since linear influence was observed in most cases, Eq. (9) is proposed to estimate $h_{c2\%}(B/2)/H_{m0}$.

$$\frac{h_{c2\%}(B/2)}{H_{m0}} = C1 + C2\,m + C3\left(\frac{R_c}{H_{m0}} - 1\right) + C4\,Ir_{m-1,0} + C5\,\frac{h_s}{H_{m0}} \geq 0 \qquad (9)$$

where $C1$, $C2$, $C3$, $C4$ and $C5$ are coefficients to be fitted for each armor layer (Cubipod®-1L, cube-2L and rock-2L). Eq. (9) is not a fully linear model, since negative values are not allowed, so conventional linear regression techniques are not adequate to determine the coefficients $C1$ to $C5$ in Eq. (9). In order to estimate $C1$ to $C5$ in Eq. (9), a nonlinear multivariable optimization algorithm without restrictions (see *The MathWorks Inc., 2019*) was used. Since this algorithm requires an initial solution to start the iterative optimization process, conventional linear regression was performed first to provide the initial solution. The final nonlinear fitting of coefficients *C1* to *C5* in Eq. (9) were calibrated by minimizing the Mean Squared Error (*MSE),* calculated as

$$MSE = \frac{1}{N_{ob}} \sum_{i=1}^{N_o} (o_i - e_i)^2 \tag{10}$$

where N_{ob} is the number of observations and o_i and e_i are the observed and estimated values. The sensitivity of the nonlinear multivariable optimization algorithm without restrictions to the initial solution was assessed. A low sensitivity of the optimization algorithm to the initial solution was observed.

Similarly to *van Gent et al.* (*2007*) and *Molines et al.* (*2018*), the bootstrapping technique was applied together with the aforementioned nonlinear optimization algorithm to characterize the variability of the coefficients in Eq. (9). The bootstrap resample technique consists in the random selection of *N* data from a dataset with *N* data, so each datum has a probability of 1/ *N* to be selected each time. Hence, some data are not selected while other data may be selected once or more than once in each resample. Using this technique, 5%, 50% and 95% percentiles were obtained for the fitted coefficients (*C1* to *C5*) and the *MSE*.

The explanatory variables were introduced one by one in the model following the structure in Eq. (11) in order to assess their significance. First, four models composed of the constant term (*C1*) and each one of the four explanatory variables were optimized. Thus, the percentage of variance explained by each model could be calculated. After that, the process was repeated keeping the explanatory variable which explained the highest percentage of the variance in the previous step and adding one of the three missing explanatory variables. This procedure was repeated until the four explanatory variables were included in the model. Once the hierarchy of the influence of each explanatory variable was obtained, the influence of the constant term (*C1*) in the explained variance was evaluated. The adjusted coefficient of determination (R^2_{adj}) defined by *Theil* (*1961*) was calculated in every step to decide if an additional explanatory variable improved the prediction model.

$$R^2_{adj} = 1 - (1 - R^2) \frac{N - 1}{N - N_P - 1} \tag{11}$$

where N is the number of data available and N_P is the number of explanatory variables. R^2_{adj} considers not only the goodness of fit but also the number of data used to fit the model. In this study, the model with the highest R^2_{adj} was selected for every armor layer; the five fitting coefficients will not always be included in the model. Figures 13 to 15 show the evolution of the median value and 90% confidence band of the R^2_{adj} depending on the number of explanatory variables considered in Eq. (9) for every armor layer model. The explanatory variable which maximized R^2_{adj} in every step, is indicated and the final number of selected explanatory variables to be included in Eq. (9) is highlighted in red.

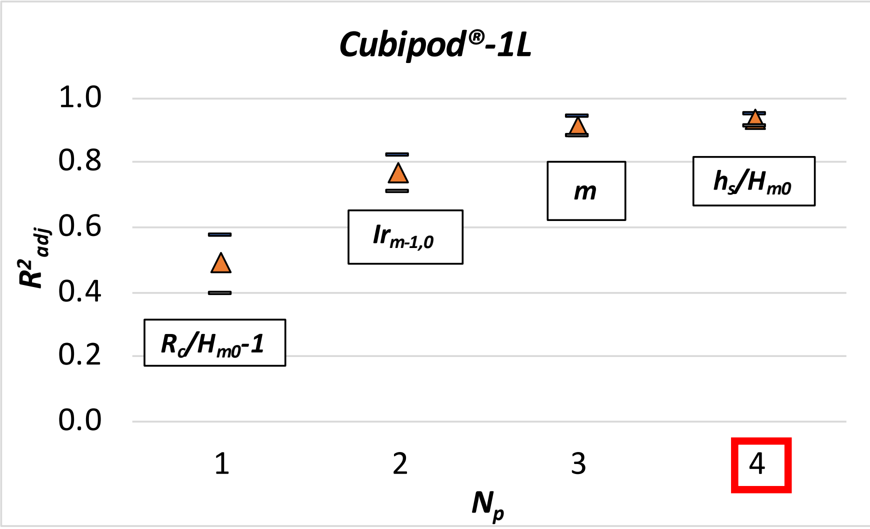

Fig. 13. Influence of the number of explanatory variables (N_p) on R^2_{adj} for Cubipod®-1L to estimate $h_{c2\%}(B/2)/H_{m0}$.

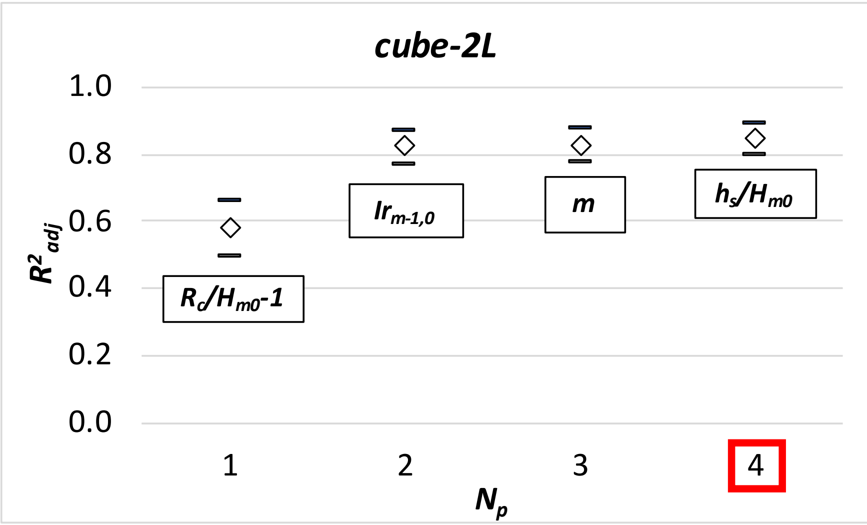

Fig. 14. Influence of the number of explanatory variables (N_p) on R^2_{adj} for cube-2L to estimate $h_{c2\%}(B/2)/H_{m0}$.

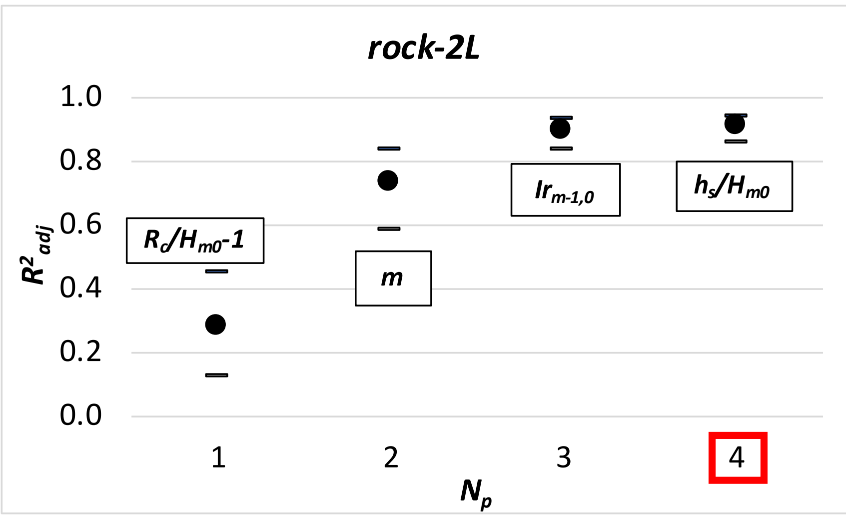

Fig. 15. Influence of the number of explanatory variables (N_p) on R^2_{adj} for rock-2L to estimate $h_{c2\%}(B/2)/H_{m0}$.

As shown in Figures 13 to 15, R_c/H_{m0} explained the highest percentage of the variance for the three armor layers. The four selected explanatory variables were significant and were included in the model. Finally, the significance of the constant term (*C1*) was assessed by repeating the optimization procedure with *C1* = 0. *C1* = 0 was proposed for Cubipod®-1L and cube-2L armors, while *C1* ≠ 0 was proposed for rock-2L armor.

The number of significant figures or significant numbers of the coefficients in the final empirical formula depended on the variability in the fitted coefficients from the bootstrapping resamples. Only one significant figure or number was reasonable for *C1*, *C2* and *C5* (coefficient of variation in the range: 7% ≤ *CV* ≤ 45%) while a maximum of two significant figures or numbers were recommended for *C3* and *C4* (4% ≤ *CV* ≤ 13%). Table 3 presents the coefficients *C1* to *C5* with the correct number of significant figures or numbers, as well as the goodness-of-fit metrics for Eq. (9) corresponding to Cubipod®-1L, cube-2L and rock-2L armors.

Figure 16 compares the measured and estimated $h_{c2\%}(B/2)/H_{m0}$ using Eq. (9) and the coefficients given in Table 3. The 90% error band is also shown in Figure 16. Good agreement is observed (R^2 = 0.876).

Armor layer	*C1*	*C2*	*C3*	*C4*	*C5*	*r*	R^2	*bias*
Cubipod®-1L	0	-4	-1/3	0.095	-0.03	0.957	0.914	0.030
cube-2L	0	-2	-0.3	0.085	-0.02	0.909	0.814	0.011
rock-2L	1/3	-10	-0.45	0.08	-0.03	0.951	0.903	0.072

Table 3. Coefficients and goodness-of-fit metrics for Eq. (9).

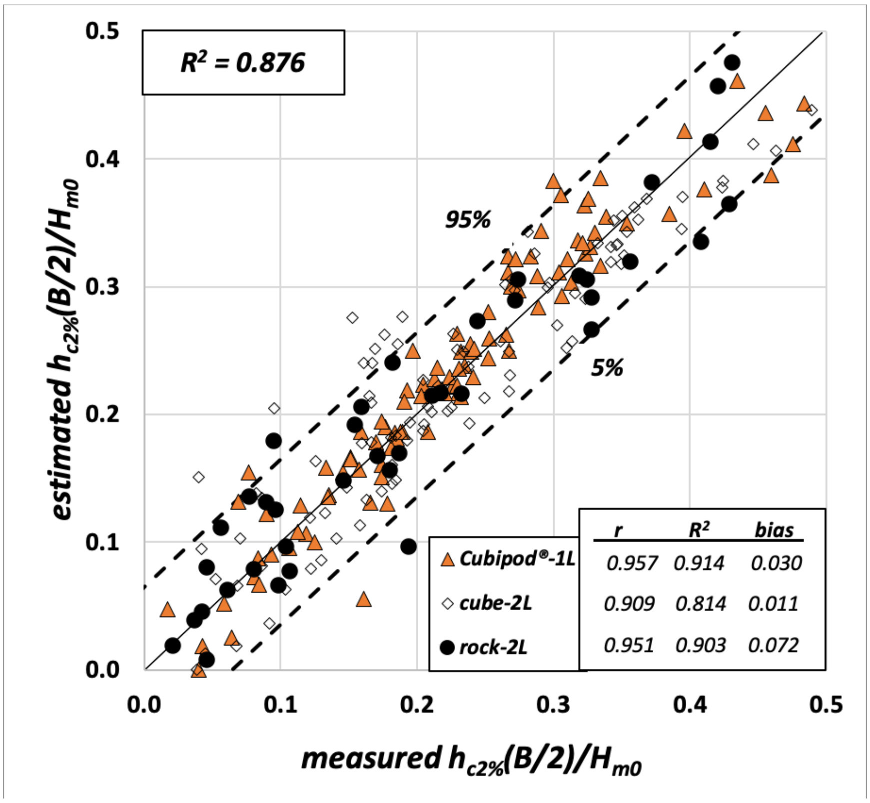

Fig. 16. Comparison between measured and estimated dimensionless $h_{c2\%}(B/2)$ *using Eq. (9) and Table 3.*

Assuming a Gaussian error distribution, the 90% error band can be estimated as

$$\left.\frac{h_{c2\%}(B/2)}{H_{m0}}\right|_{5\%}^{95\%} = \frac{h_{c2\%}(B/2)}{H_{m0}} \pm 1.64\sqrt{var(\varepsilon)} = \frac{h_{c2\%}(B/2)}{H_{m0}} \pm 0.064 \qquad (12)$$

5.2. Distribution function for extreme values of overtopping layer thickness (OLT)

As much the assessment of pedestrians' safety on mound breakwater crests as the hydraulic stability of the armor layer of mound breakwater crests require a detailed description of extreme overtopping events. Thus, the OLT distribution in the most severe wave storms must be known for the breakwater design. *Hughes et al.* (*2012*) pointed out that the extreme tail of a distribution is best described when only considering the low probability exceedance events. Hence, the distribution function of $h_c(B/2)$ with exceedance probabilities below 2% is studied here.

As reported in *Mares-Nasarre et al.* (*2019*), the best results when describing the distribution function of $h_c(B/2)$ with exceedance probabilities below 2% were obtained with a 1-parameter Exponential distribution,

$$F\left(\frac{h_c(B/2)}{h_{c2\%}(B/2)}\right) = 1 - exp\left(-C_h \frac{h_c(B/2)}{h_{c2\%}(B/2)}\right) \tag{13}$$

where $h_c(B/2)$ is the OLT value with exceedance probabilities under 2% and C_h is an empirical coefficient to be calibrated. *Mares-Nasarre et al.* (*2019*) proposed C_h = 4.2 when m = 2%. C_h was calibrated for each physical test using the 20 (1,000 waves × 2%) highest OLT measured values. $h_{c2\%}(B/2)$ estimated with Eq. (9) and coefficients in Table 3 was used in this study. The exceedance probability assigned to each OLT measured value was calculated as $N_m/(N_w+1)$, where N_m is the rank of the OLT measured value and N_w is the number of waves. The initial calibrated coefficients were C_h = 4.04 for m = 2% and C_h = 3.91 for m = 4%. The non-parametric Mood Median Test was conducted to determine if the difference between these median values of C_h was significant; the null hypothesis (H_0) corresponded to both medians being equal. Since H_0 was not rejected with a significance level α = 0.05, the final value C_h = 4 was proposed for both bottom slopes. The bottom slope does not have an influence on C_h but it does influence the estimation of $h_{c2\%}(B/2)$. Figure 17 compares measured and estimated $h_c(B/2)$ using Eq. (13) with C_h = 4. The 90% error band is also presented. Each alignment in Figure 17 corresponds to the data for one test. A good agreement (R^2 = 0.803) was obtained.

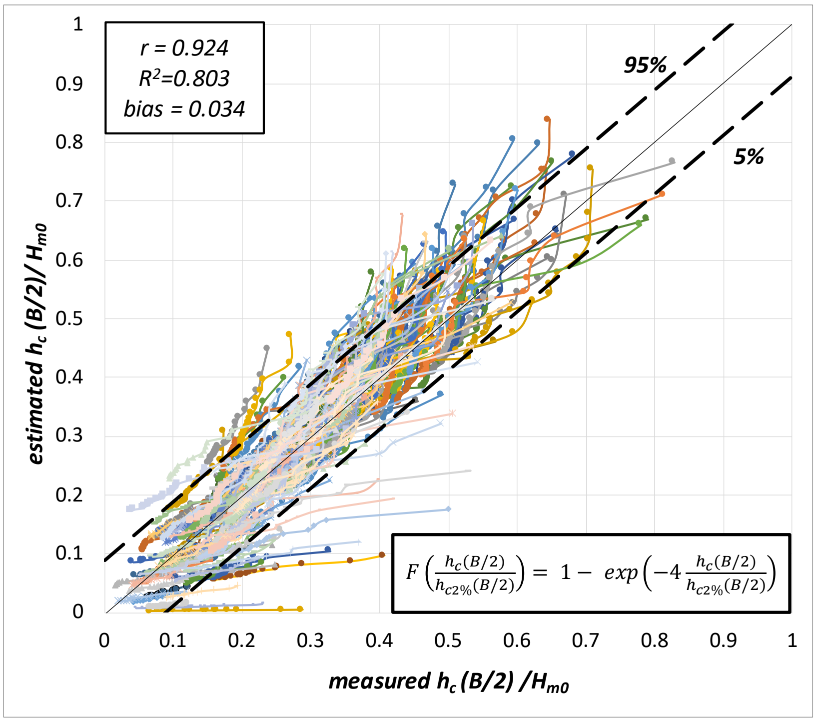

Fig. 17. Comparison between measured and estimated dimensionless $h_c(B/2)$ *using Eq. (13) with* C_h = *4.*

Assuming a Gaussian error distribution, the 90% error band can be estimated as

$$\left.\frac{h_c(B/2)}{H_{m0}}\right|_{5\%}^{95\%} = \frac{h_c(B/2)}{H_{m0}} \pm 0.087 \tag{14}$$

Figure 18 illustrates the fitting of two sample datasets to the proposed 1-parameter Exponential distribution in an exponential plot.

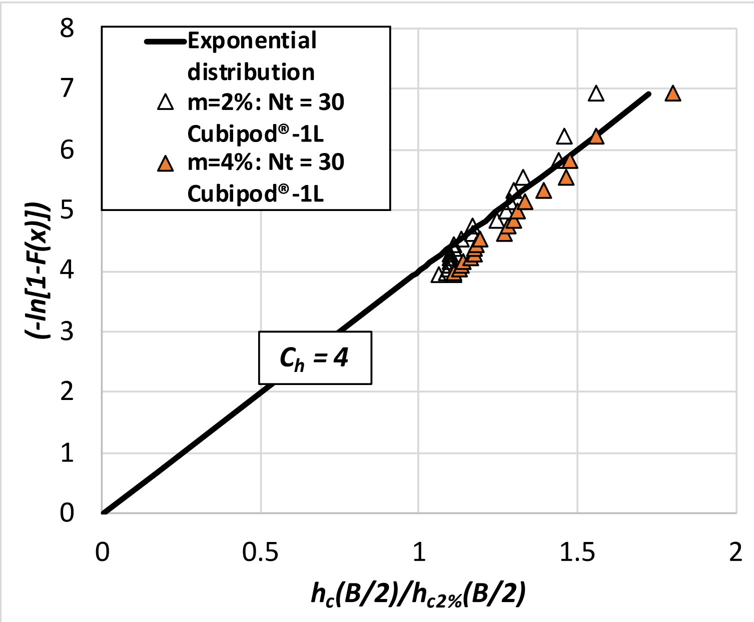

Fig. 18. Example of cumulative distribution function of $h_c(B/2)$ *in equivalent probability plot.*

6. Estimating overtopping flow velocity (OFV) on mound breakwaters

6.1. Overtopping flow velocity (OFV) exceeded by 2% of incoming waves

In Section 2, methods found in the literature to estimate OFV exceeded by 2% of the incoming waves, $u_{c2\%}(B/2)$, were described. Most of them (*Mares-Nasarre et al., 2019; Schüttrumpf and Van Gent, 2003*) were based on the correlation between the statistics of OLT and OFV. This means that $h_{c2\%}(B/2)$ needs to be estimated first with the subsequent accumulated errors later. In this study, a new formula was developed using the experimental database and considering the four input dimensionless explanatory variables described in Section 4 (m, R_c/H_{m0}, $Ir_{m-1,0}$ and h_s/H_{m0}).

Based on the trends observed in the simulations conducted with the NN models in Section 4.4, the following 5-parameter formula is proposed to estimate $u_{c2\%}(B/2)/(H_{m0}/T_{m-1,0})$

$$\frac{u_{c2\%}(B/2)}{\left(\frac{H_{m0}}{T_{m-1,0}}\right)} = D1 + D2\,m + D3\left(\frac{R_c}{H_{m0}} - 1\right) + D4\,{Ir_{m-1,0}}^2 + D5\,\frac{h_s}{H_{m0}} \geq 0 \tag{15}$$

where $D1$, $D2$, $D3$, $D4$ and $D5$ are coefficients to be calibrated. The procedure described in Section 5.1 is performed in order to assess the significance of the four explanatory variables. Figures 19 to 21 show the evolution of the median value and 90% confidence band of the R^2_{adj} depending on the number of explanatory variables considered in Eq. (15) for each armor layer model. The explanatory variable which maximized R^2_{adj} in each step is indicated and the final number of selected explanatory variables to be included in Eq. (15) is highlighted in red.

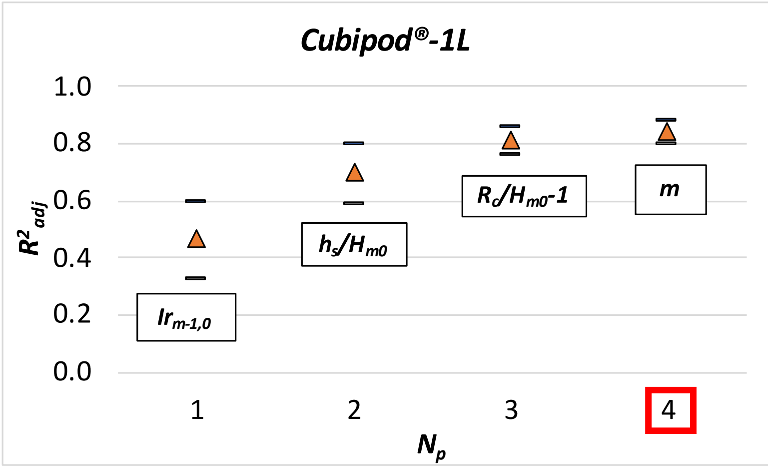

Fig. 19. Influence of the number of explanatory (N_p) variables on R^2_{adj} for Cubipod®-1L to estimate $u_{c2\%}(B/2)/(H_{m0}/T_{m-1,0})$

.

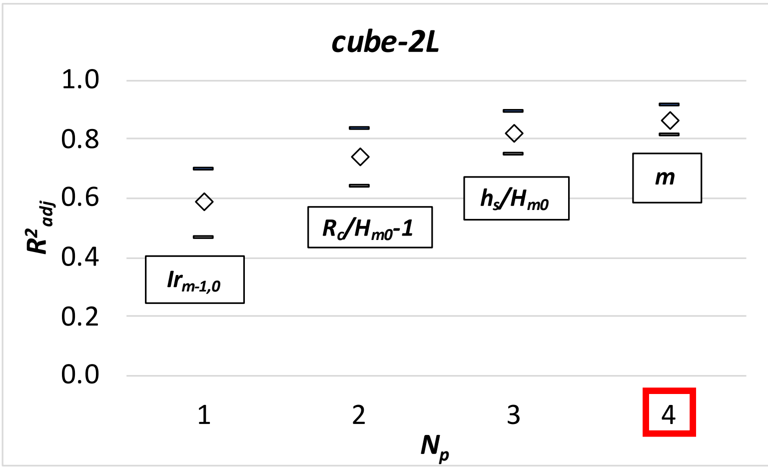

Fig. 20. Influence of the number of explanatory (N_p) variables on R^2_{adj} for cube-2L to estimate $u_{c2\%}(B/2)/(H_{m0}/T_{m-1,0})$

.

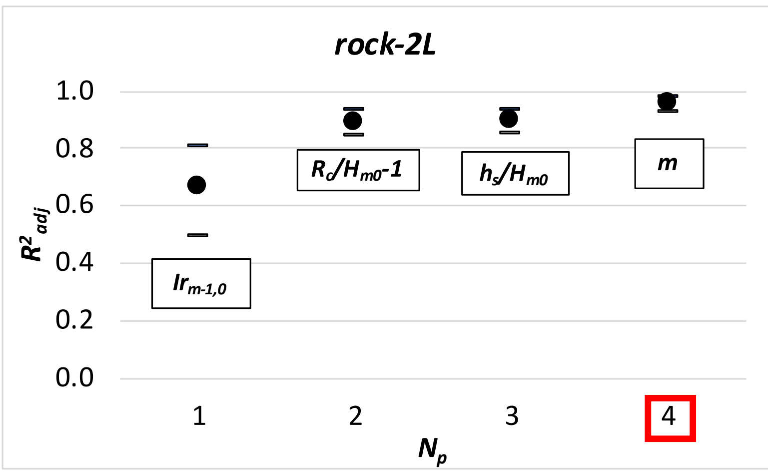

Fig. 21. Influence of the number of explanatory (N_p) variables on R^2_{adj} for rock-2L to estimate $u_{c2\%}(B/2)/(H_{m0}/T_{m-1,0})$

.

The explanatory variable $Ir_{m-1,0}$ explained the highest percentage of the variance. All the explanatory variables were significant and were included in the model. Finally, the significance of the constant term ($D1$) was assessed; $D1 \neq 0$ was proposed for the three armor layers.

The number of significant figures in the empirical coefficients in the fitted model is based on their variability from the bootstrapping resamples. One significant figure was proposed for $D1$, $D2$, $D3$ and $D5$ ($9\% \leq CV \leq 40\%$) whereas a maximum of two significant figures were recommended for $D4$ ($5\% \leq CV \leq 9\%$). Table 4 lists the final coefficients as well as the goodness-of-fit metrics for Eq. (15) corresponding to the three armor layers.

Armor layer	*D1*	*D2*	*D3*	*D4*	*D5*	*r*	*R*²	*bias*
Cubipod®-1L	2	20	-2	0.20	-1	0.920	0.832	-0.014
cube-2L	4	-30	-2	0.20	-1	0.917	0.845	0.011
rock-2L	2	-30	-3	0.25	-0.5	0.972	0.934	-0.023

Table 4. Coefficients and goodness-of-fit metrics for Eq. (15).

The measured and estimated $u_{c2\%}(B/2)/(H_{m0}/T_{m-1,0})$ with Eq. (15) using the coefficients given in Table 4 in shown in Figure 22. The 90% error band is also indicated. The agreement was good (R^2 = 0.866).

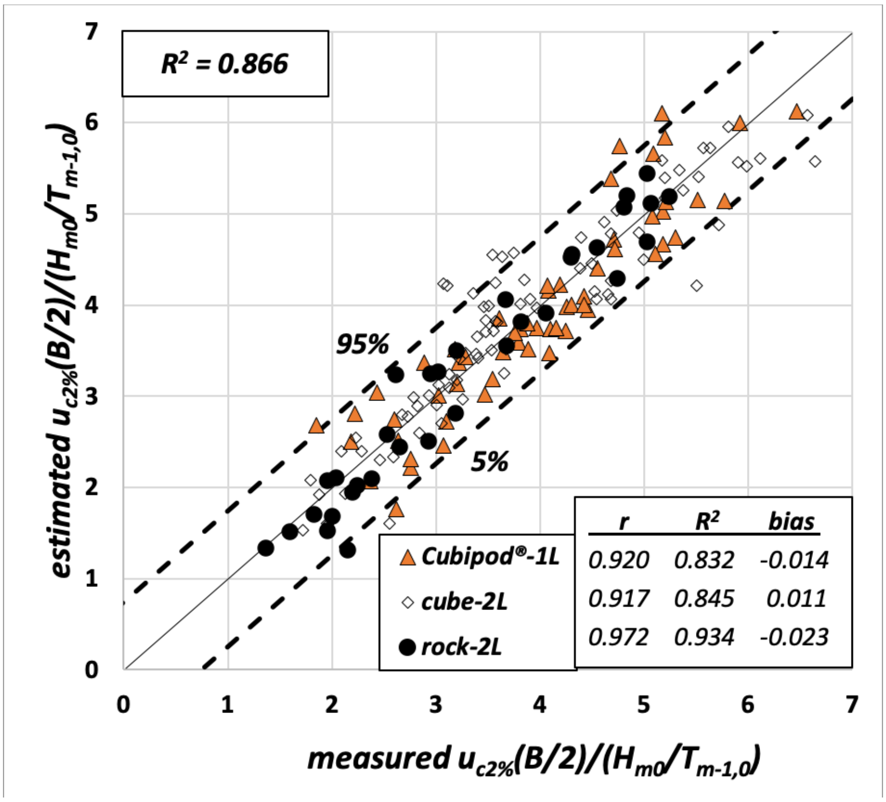

Fig. 22. Comparison between measured and estimated dimensionless $u_{c2\%}(B/2)$ *using Eq. (15) and Table 4.*

Assuming a Gaussian error distribution, the 90% error band can be estimated as

$$\left.\frac{u_{c2\%}(B/2)}{(H_{m0}/T_{m-1,0})}\right|_{5\%}^{95\%} = \frac{u_{c2\%}(B/2)}{(H_{m0}/T_{m-1,0})} \pm 0.744 \qquad (16)$$

6.2. Distribution function for extreme values of overtopping flow velocity (OFV)

Similar to Section 5.2, the OFV events during the most severe wave storms are characterized here. Thus, the distribution function of $u_c(B/2)$ with exceedance probabilities below 2% was studied in this section. *Mares-Nasarre et al.* (*2019*) recommended the Rayleigh distribution to describe the distribution function of $u_c(B/2)$ with exceedance probabilities below 2%. Here, best results were also obtained with the Rayleigh distribution given as

$$F\left(\frac{u_c(B/2)}{u_{c2\%}(B/2)}\right) = 1 - exp\left(-C_u\left[\frac{u_c(B/2)}{u_{c2\%}(B/2)}\right]^2\right) \tag{17}$$

where C_u is an empirical coefficient to be calibrated. *Mares-Nasarre et al.* (*2019*) proposed C_u =3.6 when m = 2%. The calibration procedure described in Section 5.2 is also applied here. Note that $u_{c2\%}(B/2)$ estimated with Eq. (15) together coefficients in Table 4 were used to simulate the design phase conditions. The initial calibrated coefficients were C_u = 3.62 for m = 2% and C_u = 3.46 for m = 4%. Since C_u values were similar for both bottom slopes, the non-parametric Mood Median Test was performed to determine if the difference between the median values of C_u was significant. The null hypothesis (H_0) corresponded to both medians being equal; H_0 was not rejected with a significance level α = 0.05. Hence, the final value C_u = 3.5 was proposed for the two bottom slopes. The bottom slope does not influence C_u but it does influence the estimation of $u_{c2\%}(B/2)$. Comparison between measured and estimated $u_c(B/2)$ using Eq. (17) with C_u = 3.5 is shown in Figure 23. The 90% error band is also indicated. A good agreement (R^2 = 0.812) was obtained.

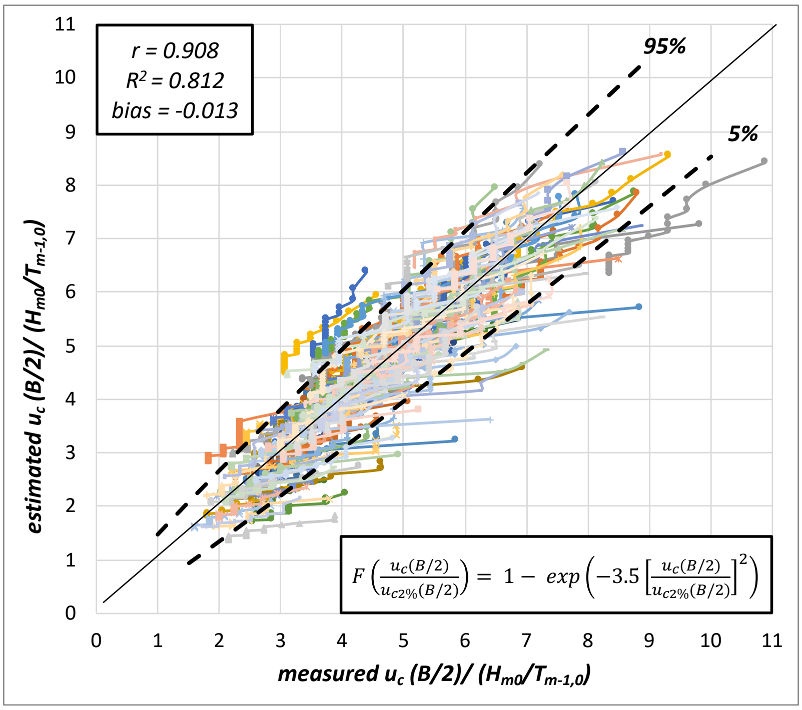

Fig. 23. Comparison between measured and estimated dimensionless $u_c(B/2)$ *using Eq. (19) with* C_u = *3.5.*

It was observed that *MSE* rose for larger values of $u_c(B/2)/(H_{m0}/T_{m-1,0})$. Thus, the methodology proposed by *Herrera and Medina* (*2015*) was used here to estimate the 90% error band. Assuming a Gaussian error (ε) distribution with 0 mean and variance calculated as

$$\sigma^2(\varepsilon) = 0.08\frac{u_c(B/2)}{(H_{m0}/T_{m-1,0})} \tag{18}$$

The 90% error band is obtained as

$$\left.\frac{u_c(B/2)}{(H_{m0}/T_{m-1,0})}\right|_{5\%}^{95\%} = \frac{u_c(B/2)}{(H_{m0}/T_{m-1,0})} \pm 0.46\sqrt{\frac{u_c(B/2)}{(H_{m0}/T_{m-1,0})}} \tag{19}$$

Figure 24 illustrates the fitting of two sample datasets in a Rayleigh probabilistic plot.

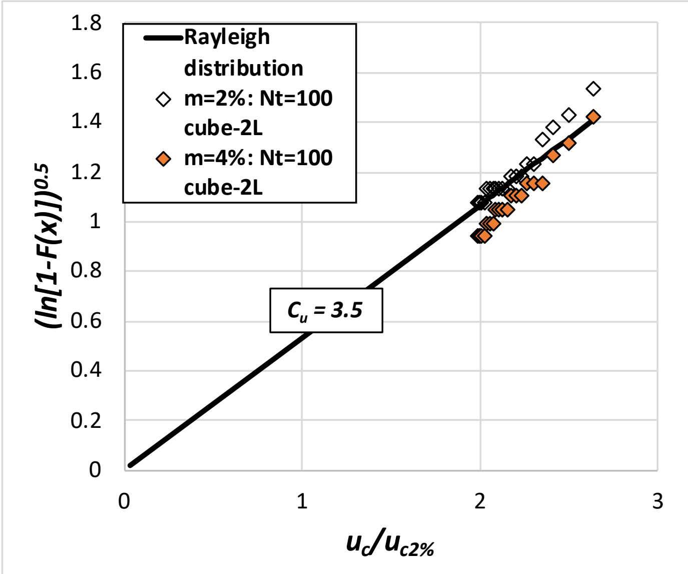

Fig. 24. Example of the cumulative distribution function of $u_c(B/2)$ *in a Rayleigh probability plot.*

7. Evaluation of the influence of the explanatory variables

As shown in Sections 5 and 6, the four selected explanatory variables (m, R_c/H_{m0}, $Ir_{m-1,0}$ and h_s/H_{m0}) were found to be significant when estimating $h_{c2\%}(B/2)$ and $u_{c2\%}(B/2)$. Nevertheless, the influence of h_s/H_{m0} on $h_{c2\%}(B/2)$ and m on $u_{c2\%}(B/2)$ was low. In this section, the performance of Eq. (9) and (15) is assessed when h_s/H_{m0} in Eq. (9) and m in Eq. (15) are disregarded. Table 5 presents the calibrated coefficients as well as the goodness-of-fit metrics for Eq. (9) when h_s/H_{m0} is not included in the model ($C5$ = 0) for the three armor layers.

Armor layer	*C1*	*C2*	*C3*	*C4*	*C5*	*r*	R^2	*bias*
Cubipod®-1L	0	-4	-1/3	0.085	0	0.949	0.900	0.008
cube-2L	0	-2	-0.3	0.075	0	0.902	0.804	0.067
rock-2L	0.3	-10	-0.45	0.075	0	0.947	0.875	0.194

Table 5. Sensitivity of the coefficients and goodness-of-fit metrics for OLT-Eq. (11) when h_s/H_{m0} *is disregarded*

When comparing Tables 3 and 5, the relative variation (Δ%) of the coefficients are: $C1$ (0 ≤ Δ% ≤ 11%), C2 (Δ%=0), C3 (Δ%=0) and $C4$ (6% ≤ Δ% ≤ 12%). Most of the coefficients gave the same values. Regarding the goodness of fit, R^2 decreased around 2% when $C5$ = 0.

Table 6 lists the calibrated coefficients as well as the goodness-of-fit metrics for Eq. (15) when m is not included in the model ($D2$ = 0) for the three armor layers.

Armor layer	*D1*	*D2*	*D3*	*D4*	*D5*	*r*	R^2	*bias*
Cubipod®-1L	3	0	-2	0.2	-1	0.909	0.785	0.068
cube-2L	2	0	-2	0.2	-0.5	0.901	0.796	-0.018
rock-2L	1	0	-3	0.2	-0.2	0.943	0.872	-0.039

Table 6. Sensitivity of the coefficients and goodness-of-fit metrics for OFV-Eq. (17) when m *is disregarded*

When comparing Tables 4 and 6, the relative variation (Δ%) of the coefficients are: D*1* (Δ% =50%), D3 (Δ%=0), D4 (0 ≤ Δ% ≤ 20%) and $D5$ (0 ≤ Δ% ≤ 50%). R^2 decreased around 6% when $D2$ = 0. Note that the influence of m is also included in the model by the wave conditions, H_{m0}. Thus, m is still relevant even if it is not an explicit explanatory variable in the model.

From the results in Tables 5 and 6, it can be concluded that the performance of Eq. (9) and (15) is still satisfactory when removing h_s/H_{m0} and m, respectively. However, it should be noted that such explanatory variables were statistically significant as described in Sections 5 and 6.

8. Conclusions

Mound breakwater design is evolving due to the social concerns about the impact of coastal structures and the rising sea levels as well as stronger wave conditions caused by climate change. These drivers of change have led to reduced design crest freeboards and increased overtopping risks. In this context, the OLT and OFV on the breakwater crest has become relevant to assess the hydraulic stability of the armored crest and the pedestrian safety on the breakwater crest.

In this study, 235 physical tests reported in *Mares-Nasarre et al.* (*2019* and *2020a*) were used to propose empirical models to estimate OLT and OFV. The 2D tests measured OLT and OFV on overtopped mound breakwaters with three armor layers (Cubipod®-1L, cube-2L and rock-2L) in depth-limited breaking wave conditions with two bottom slopes (m = 2% and m = 4%) and armor slope $\tan\alpha$=2/3.

Sea bottom slope, dimensionless crest freeboard, Iribarren number related to wave steepness and dimensionless water depth (m, R_c/H_{m0}, $Ir_{m-1,0}$ and h_s/H_{m0}) were the selected explanatory variables to estimate OLT and OFV exceeded by 2% of the incoming waves in the middle of the breakwater crest, $h_{c2\%}(B/2)$ and $u_{c2\%}(B/2)$. Eqs. (11) and (17) with five coefficients are proposed to estimate dimensionless OLT ($h_{c2\%}(B/2)/H_{m0}$) and OFV ($u_{c2\%}(B/2)/(H_{m0}/T_{m-1,0})$, respectively, using the four dimensionless explanatory variables. The coefficients to be used in Eqs. (9) and (15), as well as the goodness-of-fit metrics for Cubipod®-1L, cube-2L and rock-2L armors, are given in Tables 3 and 4, respectively; the agreement between measured and estimated $h_{c2\%}(B/2)$ and $u_{c2\%}(B/2)$ was good ($0.866 \leq R^2 \leq 0.876$)

Dimensionless crest freeboard, R_c/H_{m0}, was the most significant explanatory variable to describe OLT whereas the Iribarren number related to wave steepness, $Ir_{m-1,0}$, was the most significant variable to describe OFV; the bottom slope (m) had a significant influence on $h_c(B/2)$ and $u_c(B/2)$.

In order to better describe the OLT and OFV during the most severe wave storms, the 1-parameter Exponential and Rayleigh distribution functions were used to estimate OLT and OFV values, respectively, with exceedance probabilities below 2%, $h_c(B/2)$ and $u_c(B/2)$. The recommended coefficients for the 1-parameter Exponential distribution and the Rayleigh distributions were C_h = 4 for Eq. (13) and C_u = 3.5 for Eq. (17), respectively; the agreement was good ($0.803 \leq R^2 \leq 0.812$) between the measured and estimated $h_c(B/2)$ and $u_c(B/2)$ given by Eqs. (13) and (17) when using C_h = 4 and C_u = 3.5, respectively.

Acknowledgements

The authors thank the three anonymous reviewers for their comments and suggestions. The authors acknowledge the financial support from the Spanish *Ministerio de Economía y Competitividad* and *Fondo Europeo de Desarrollo Regional* (FEDER) under grant RTI2018-101073-B-I00. The first author was also financially supported through the FPU program (*Formación de Profesorado Universitario*) funded by the Spanish *Ministerio de Educación, Cultura y Deporte* under grant FPU16/05081. The authors thank Debra Westall for revising the manuscript.

Appendix A. Data used in this study: $h_{c2\%}(B/2)$ and $u_{c2\%}(B/2)$

This appendix provides the test matrix used in this study as well as the observed OLT and OFV exceeded by 2% of the incoming waves in the middle of the breakwater crest ($h_{c2\%}(B/2)$ and $u_{c2\%}(B/2)$, respectively). Wave runs of N_w = 1,000 waves were generated following a JONSWAP spectrum (γ = 3.3). m represents the bottom slope, H_{m0} and $T_{m-1,0}$ are the incident spectral significant wave height and the spectral period at a distance of 3 times the water depth from the toe of the structure, R_c is the crest freeboard and h_s is the water depth at the toe of the structure. Tables 7 to 9 present the data from the tests performed with the models with Cubipod®-1L, cube-2L and rock-2L, respectively.

Test #	m (%)	H_{m0} (mm)	$T_{m-1,0}$ (s)	R_c (mm)	h_s (mm)	$h_{c2\%}(B/2)$ (mm)	$u_{c2\%}(B/2)$
1	2	93	1.04	120	200	6	-
2	2	101	1.12	121	200	8	-
3	2	107	1.13	121	200	11	-
4	2	112	1.12	121	200	13	-
5	2	119	1.19	121	200	16	-
6	2	125	1.22	122	200	18	-
7	2	129	1.25	122	200	19	-
8	2	133	1.30	122	200	21	-
9	2	135	1.31	122	200	24	-
10	2	136	1.28	122	200	25	-
11	2	142	1.41	122	200	27	-
12	2	142	1.40	120	200	29	-
13	2	143	1.42	120	200	30	-
14	2	76	1.42	120	200	12	-
15	2	102	1.59	120	200	18	-
16	2	111	1.59	120	200	23	-
17	2	118	1.63	121	200	28	-
18	2	125	1.64	121	200	33	-
19	2	133	1.73	121	200	33	-
20	2	136	1.85	122	200	39	-
21	2	140	1.86	123	200	37	-
22	2	142	1.88	120	200	40	-
23	2	145	1.88	121	200	39	-
24	2	147	1.87	122	200	40	-
25	2	149	1.98	123	200	43	-
26	2	75	0.93	70	250	8	-
27	2	84	1.03	70	250	13	-
28	2	91	1.04	70	250	17	230
29	2	102	1.10	70	250	23	255
30	2	110	1.08	71	250	26	279
31	2	117	1.11	71	250	29	279
32	2	124	1.16	71	250	33	279
33	2	133	1.23	71	250	38	327
34	2	138	1.26	72	250	42	352
35	2	145	1.33	73	250	44	352
36	2	152	1.38	74	250	47	352
37	2	157	1.40	75	250	51	425
38	2	162	1.46	77	250	52	425
39	2	164	1.45	78	250	53	425
40	2	167	1.47	80	250	54	449
41	2	76	1.42	71	250	15	-
42	2	88	1.52	72	250	24	-
43	2	99	1.62	70	250	35	-
44	2	109	1.62	70	250	42	-
45	2	118	1.68	71	250	48	-

46	2	128	1.72	72	250	59	-
47	2	137	1.84	70	250	54	-
48	2	145	1.92	72	250	66	-
49	2	149	1.83	74	250	71	-
50	2	155	1.90	70	250	81	-
51	2	160	1.97	70	250	80	-
52	2	164	1.94	71	250	79	-
53	2	167	2.04	71	250	73	-
54	4	100	1.04	120	200	4	-
55	4	109	1.12	120	200	5	-
56	4	116	1.18	120	200	7	182
57	4	123	1.19	120	200	10	230
58	4	129	1.24	120	200	12	255
59	4	139	1.32	120	200	12	303
60	4	142	1.33	120	200	16	352
61	4	147	1.34	120	200	20	400
62	4	155	1.41	121	200	21	449
63	4	156	1.40	121	200	25	473
64	4	160	1.41	122	200	28	473
65	4	165	1.48	122	200	28	498
66	4	91	1.60	120	200	8	206
67	4	103	1.64	120	200	18	255
68	4	113	1.76	120	200	21	303
69	4	121	1.74	121	200	25	327
70	4	130	1.87	120	200	29	400
71	4	136	1.88	121	200	29	400
72	4	142	1.77	122	200	33	425
73	4	151	1.74	120	200	35	449
74	4	158	1.71	122	200	35	473
75	4	79	0.94	70	250	1	-
76	4	85	1.18	70	250	6	157
77	4	89	1.03	70	250	11	206
78	4	98	1.08	70	250	16	279
79	4	108	1.10	70	250	19	303
80	4	116	1.15	70	250	21	352
81	4	124	1.17	70	250	23	376
82	4	130	1.26	71	250	25	425
83	4	136	1.24	70	250	32	425
84	4	146	1.33	71	250	34	425
85	4	154	1.39	72	250	36	473
86	4	161	1.39	73	250	39	498
87	4	168	1.43	75	250	40	522
88	4	175	1.48	77	250	40	498
89	4	180	1.48	80	250	46	498
90	4	69	1.42	70	250	5	-
91	4	80	1.53	70	250	18	230
92	4	89	1.60	70	250	22	255
93	4	101	1.73	70	250	28	303
94	4	111	1.72	70	250	35	327
95	4	119	1.76	71	250	40	352
96	4	132	1.90	70	250	45	352
97	4	138	1.84	70	250	46	352
98	4	150	2.06	72	250	50	376
99	4	157	1.98	74	250	50	376
100	4	166	2.04	77	250	54	425

101	4	174	2.15	81	250	52	522
102	4	180	2.14	86	250	55	498

Table 7. Data from the tests conducted with the Cubipod®-1L armored model.

Test #	*m* (%)	H_{m0} (mm)	$T_{m-1,0}$ (s)	R_c (mm)	h_s (mm)	$h_{c2\%}(B/2)$ (mm)	$u_{c2\%}(B/2)$ (mm/s)
1	2	67	0.95	112	250	3	-
2	2	75	0.99	112	250	6	-
3	2	85	1.05	112	250	12	157
4	2	85	1.05	112	250	12	206
5	2	101	1.08	112	250	16	230
6	2	108	1.10	111	250	20	279
7	2	117	1.17	111	250	21	279
8	2	127	1.26	112	250	22	327
9	2	134	1.25	112	250	24	352
10	2	142	1.34	112	250	25	376
11	2	147	1.38	112	250	29	425
12	2	153	1.38	113	250	28	425
13	2	157	1.40	111	250	25	376
14	2	160	1.45	112	250	31	425
15	2	69	1.43	111	250	3	-
16	2	81	1.57	112	250	15	-
17	2	94	1.58	112	250	25	230
18	2	104	1.63	112	250	28	279
19	2	113	1.79	111	250	33	327
20	2	122	1.72	111	250	39	327
21	2	132	1.87	112	250	45	376
22	2	140	1.90	112	250	49	449
23	2	144	1.90	113	250	41	449
24	2	150	1.91	115	250	59	522
25	2	157	2.04	116	250	58	643
26	2	163	2.05	111	250	69	522
27	2	67	0.89	61	300	6	-
28	2	75	0.94	61	300	12	-
29	2	83	0.99	61	300	19	-
30	2	92	1.02	61	300	25	206
31	2	100	1.07	62	300	31	255
32	2	109	1.12	62	300	33	303
33	2	115	1.03	62	300	36	327
34	2	124	1.17	62	300	40	376
35	2	129	1.22	62	300	42	376
36	2	139	1.28	63	300	48	376
37	2	145	1.27	63	300	51	400
38	2	153	1.34	64	300	53	352
39	2	162	1.43	61	300	57	400
40	2	166	1.42	63	300	57	425
41	2	172	1.43	64	300	62	449
42	2	178	1.50	66	300	64	522
43	2	69	1.42	68	300	18	-
44	2	80	1.52	61	300	28	-
45	2	92	1.63	61	300	36	279
46	2	101	1.63	61	300	43	352
47	2	112	1.78	62	300	50	376
48	2	119	1.75	63	300	55	376
49	2	130	1.89	61	300	64	400

50	4	106	1.14	161	200	4	182
51	4	114	1.18	161	200	8	182
52	4	120	1.18	161	200	11	182
53	4	125	1.27	161	200	13	206
54	4	132	1.27	161	200	16	230
55	4	139	1.33	161	200	19	279
56	4	144	1.34	161	200	23	303
57	4	151	1.39	161	200	25	327
58	4	154	1.40	161	200	27	352
59	4	158	1.41	161	200	29	352
60	4	162	1.47	161	200	29	376
61	4	102	1.63	161	200	9	-
62	4	112	1.70	161	200	15	230
63	4	120	1.74	161	200	22	279
64	4	131	1.87	161	200	26	352
65	4	136	1.80	162	200	28	352
66	4	146	1.76	162	200	30	376
67	4	152	1.72	162	200	36	400
68	4	158	1.73	161	200	33	425
69	4	163	1.70	162	200	36	449
70	4	166	1.76	163	200	42	522
71	4	97	1.06	111	250	5	157
72	4	106	1.10	111	250	7	206
73	4	115	1.17	111	250	10	255
74	4	123	1.24	111	250	15	303
75	4	130	1.30	111	250	24	327
76	4	136	1.24	111	250	26	327
77	4	146	1.33	111	250	30	400
78	4	154	1.39	112	250	33	376
79	4	161	1.39	112	250	33	425
80	4	168	1.43	112	250	40	400
81	4	175	1.48	113	250	41	425
82	4	180	1.48	114	250	41	425
83	4	89	1.60	111	250	3	-
84	4	101	1.73	111	250	9	182
85	4	111	1.72	111	250	17	230
86	4	119	1.76	111	250	27	303
87	4	132	1.90	111	250	34	327
88	4	138	1.84	112	250	39	352
89	4	150	2.06	111	250	43	376
90	4	157	1.98	112	250	41	425
91	4	166	2.04	114	250	43	425
92	4	174	2.15	117	250	56	449
93	4	180	2.14	111	250	61	473

Table 8. Data from the tests conducted with the cube-2L armored model.

Test #	m (%)	H_{m0} (mm)	$T_{m-1,0}$ (s)	R_c (mm)	h_s (mm)	$h_{c2\%}(B/2)$ (mm)	$u_{c2\%}(B/2)$ (mm/s)
1	2	105	1.13	151	200	6	-
2	2	110	1.12	152	200	8	133
3	2	117	1.17	151	200	11	182
4	2	86	1.50	151	200	8	-
5	2	98	1.59	151	200	18	182
6	2	108	1.58	151	200	23	206
7	2	117	1.70	152	200	28	279

8	2	122	1.67	152	200	33	279
9	2	72	0.89	102	250	3	-
10	2	81	0.99	101	250	14	-
11	2	89	1.01	102	250	19	-
12	2	98	1.06	101	250	32	206
13	2	108	1.12	101	250	39	255
14	2	114	1.11	101	250	47	303
15	2	121	1.17	102	250	52	327
16	2	74	1.42	101	250	17	-
17	2	85	1.52	101	250	28	206
18	2	98	1.62	101	250	36	303
19	2	108	1.62	101	250	45	303
20	2	116	1.73	101	250	49	352
21	2	126	1.72	101	250	54	352
22	4	123	1.25	151	200	3	157
23	4	130	1.26	151	200	5	206
24	4	137	1.31	151	200	15	230
25	4	143	1.34	151	200	15	255
26	4	102	1.69	151	200	5	157
27	4	112	1.73	151	200	7	206
28	4	120	1.74	151	200	23	255
29	4	130	1.89	151	200	23	327
30	4	91	1.08	101	250	3	182
31	4	100	1.08	101	250	8	182
32	4	109	1.18	101	250	10	182
33	4	116	1.15	101	250	17	206
34	4	126	1.26	101	250	19	255
35	4	89	1.53	101	250	9	-
36	4	101	1.70	101	250	16	255
37	4	111	1.72	101	250	20	279
38	4	124	1.91	101	250	34	327
39	4	129	1.86	101	250	41	352
40	4	138	1.90	102	250	43	352

Table 9. Data of the tests conducted with the rock-2L armored model.

Notation

Acronyms:

AWACS = Active Wave Absorption System

bias = Relative bias

LASA-V = Local Approximation using Simulated Annealing (*Figueres and Medina, 2005*)

LPC-UPV = Laboratory of Ports and Coasts (UPV)

MSE = Mean squared error

MWL = Mean water level

NN = Neural Network

OLT = Overtopping layer thickness

OFV	= Overtopping flow velocity
r	= Correlation coefficient
R^2	= Coefficient of determination
R^2_{adj}	= Adjusted coefficient of determination
UPV	= Universitat Politècnica de València (ES)

<u>Symbols:</u>

B	= crest width
$cot\alpha$ [-]	= armor slope
$Dn50$ [m] or [cm]	= $(W_{50}/\rho)^{1/3}$, nominal diameter
e_i	= estimated values
$\bar{e}$	= average of the estimated values
g [m/s²]	= gravitational acceleration
h_s [m] or [cm]	= water depth
$h_{A2\%}(z_A)$ [m] or [cm]	= run-up layer thickness exceeded by 2% of the incoming waves
$h_c(x_c)$ [m] or [cm]	= overtopping layer thickness with exceedance probabilities below 2%
$h_{c2\%}(x_c)$ [m] or [cm]	= overtopping layer thickness exceeded by 2% of the incoming waves
H_{m0} [m] or [cm]	$=4(m_0)^{0.5}$, spectral wave height
$H_{m0,g}$ [m] or [cm]	= spectral wave height in the wave generation zone
$H_{m0,i}$ [m] or [cm]	= incident spectral wave height
$H_{m0,m}$ [m] or [cm]	= measured spectral wave height
$H_{m0,r}$ [m] or [cm]	= reflected spectral wave height
H_s [m] or [cm]	= significant wave height or average wave height of the highest one-third waves, $H_{1/3}$
$Ir_{m-1,0}$ [-]	= $\xi_{-1,0} = tan\alpha/(H_{m0}/L_{m-1,0})^{0.5}$, Iribarren number or surf similarity parameter calculated with H_{m0} and $T_{m-1,0}$
K_r [-]	= $H_{m0,r}/ H_{m0,i}$, reflection coefficient

$L_{m-1,0}$ [m] or [cm]	$= gT_{m-1,0}^2/2\pi$, deep water wave length based on the spectral period, $T_{m-1,0}$
L_{0p} [m] or [cm]	$= gT_p^2/2\pi$, deep water wave length based on the peak period, T_p
m [-]	= bottom slope
m_i	= i-th spectral moment
N_h [-]	= number of neurons in the hidden layer of NNs
N_i [-]	= number of neurons in the input layer of NNs
N_o [-]	= number of neurons in the output layer of NNs
N_{ob} [-]	= number of observations
o_i	= observed values
P [-]	= number of free parameters in NNs
R_c [m] or [cm]	= crest freeboard
$Ru_{2\%}$ [m] or [cm]	= wave run-up height exceeded by 2% of the incoming waves
s_{0p} [-]	$=H_{s0}/L_{0p}$, deep water wave steepness based on the peak period, T_{p0}
$S(f)$	= wave spectrum
t [s]	= time
$T_{m-1,0}$ [s]	$= m_{-1}/m_0$, spectral wave period based on the spectral moment, m_{-1}
T_p [s]	= peak wave period
T_{p0} [s]	= deep waters peak wave period
T-BLIND [-]	= subset used for blind testing
TEST [-]	= 15%*TR*, subset used for cross validation of the trained NNs as part of the Early Stopping Criterion
TR [-]	= subset used for training NNs
TRAIN [-]	= 70%*TR*, subset used for the formal training of NNs as part of the Early Stopping Criterion
VAL [-]	= 15%*TR*, subset used for validation during the training of NNs as part of the Early Stopping Criterion

$u_{A2\%}(z_A)$ [m/s] or [cm/s]	= run-up velocity
$u_c(x_c)$ [m/s] or [cm/s]	= overtopping velocity with exceedance probabilities below 2%
$u_{c2\%}(x_c)$ [m/s] or [cm/s]	= overtopping velocity exceeded by 2% of the incoming waves
x_c [m] or [cm]	= horizontal coordinate along the crest from the seaward edge
x_e	= estimated value given by the linear regression
z_A [m] or [cm]	= elevation on the MWL
ε [-]	= error, difference between the estimated and the measured value
α [º] or [rad]	= angle of the slope
$\Delta\%$	= relative variation of the empirical coefficients
γ [-]	= parameter of the JONSWAP spectrum
γ_b [-]	= berm factor
γ_f [-]	= roughness factor
γ_β [-]	= obliquity factor
μ [-]	= friction factor of dike crests according to *Schüttrumpf et al. (2002*)

References

Abt, S.R., Wittier, R.J., Taylor, A., Love, D.J., *1989*. Human stability in a high flood hazard zone. JAWRA J. Am. Water Resour. Assoc. 25, 881–890. https://doi.org/10.1111/j.1752-1688.1989.tb05404.x

Argente, G., Gómez-Martín, M.E., Medina, J.R., *2018*. Hydraulic stability of the armor layer of overtopped breakwaters. J. Mar. Sci. Eng. 6, 1–13. https://doi.org/10.3390/jmse6040143

Bae, H.U., Yun, K.M., Yoon, J.Y., Lim, N.H., *2016*. Human stability with respect to overtopping flow on the breakwater. Int. J. Appl. Eng. Res. 11, 111–119.

Battjes, J.A., Groenendijk, H.W., *2000*. Wave height distributions on shallow foreshores. Coast. Eng. 40, 161–182. https://doi.org/10.1016/S0378-3839(00)00007-7

Camus, P., Tomás, A., Díaz-Hernández, G., Rodríguez, B., Izaguirre, C., Losada, I.J., *2019*. Probabilistic assessment of port operation downtimes under climate change. Coast. Eng. 147, 12–24. https://doi.org/10.1016/j.coastaleng.2019.01.007

Endoh, K., Takahashi, S., *1995*. Numerically modeling personnel danger on a promenade breakwater due to overtopping waves, in: Proc. 24th International Conference on Coastal Engineering. pp. 1016–1029.

EurOtop. A manual on wave overtopping of sea defences and related structures. An overtopping manual largely based on European research but for worldwide Application, *2018*. Van der Meer, J. W.; Allsop, N.W.H.; Bruce, T.; De Rouck, J.; Kortenhaus, A.; Pullen, T.; Schüttrumpf, H.; Troch, P.; Zanuttigh, B. www.overtopping-manual.com.

Figueres, M., Medina, J.R., *2005*. Estimating incident and reflected waves using a fully nonlinear wave model, in: Proc. 29th International Conference on Coastal Engineering. Lisboa (Portugal), pp. 594–603. https://doi.org/10.1142/9789812701916-0047

Formentin, S.M., Gaeta, M.G., Palma, G., Zanuttigh, B., Guerrero, M., *2019*. Flow Depths and Velocities across a Smooth Dike Crest. Water 11, 2197. https://doi.org/10.3390/w11102197

Formentin, S.M., Zanuttigh, B., van der Meer, J.W., *2017*. A Neural Network Tool for Predicting Wave Reflection, Overtopping and Transmission. Coast. Eng. J. 59, 1750006-1-1750006–31. https://doi.org/10.1142/S0578563417500061

Goda, Y., *1985*. Random Seas and Design of Maritime Structures. University of Tokyo Press, Tokyo, Japan.

Gómez-Martín, M.E., Medina, J.R., *2014*. Heterogeneous Packing and Hydraulic Stability of Cube and Cubipod Armor Units. J. Waterw. Port, Coastal, Ocean Eng. 140, 100–108. https://doi.org/10.1061/(ASCE)WW.1943-5460.0000223

Herrera, M.P., Gómez-Martín, M.E., Medina, J.R., *2017*. Hydraulic stability of rock armors in breaking wave conditions. Coast. Eng. 127, 55–67. https://doi.org/10.1016/j.coastaleng.2017.06.010

Herrera, M.P., Medina, J.R., *2015*. Toe berm design for very shallow waters on steep sea bottoms. Coast. Eng. 103, 67–77. https://doi.org/10.1016/j.coastaleng.2015.06.005

Hughes, S.A., Thornton, C.I., Van der Meer, J.W., Scholl, B., *2012*. Improvements in describing wave overtopping processes. Proc. 33rd Int. Conf. Coast. Eng. [SI], 1–15. https://doi.org/10.9753/icce.v33.waves.35

Lorke, S., Scheres, B., Schüttrumpf, H., Bornschein, A., Pohl, R., *2012*. Physical model tests on wave overtopping and flow processes on dike crests influenced by wave-current interaction. Coast. Eng. Proc. 1–13. https://doi.org/10.9753/icce.v33.waves.34

Mansard, E.P.D., Funke, E.R., *1980*. The Measurement of Incident and Reflected Spectra Using a Least squares Method, in: Proc. 17th International Conference on Coastal Engineering. ASCE, pp. 154–172.

Mares-Nasarre, P., Argente, G., Gómez-Martín, M.E., Medina, J.R., *2019*. Overtopping layer thickness and overtopping flow velocity on mound breakwaters. Coast. Eng. 154, 103561. https://doi.org/10.1016/J.COASTALENG.2019.103561

Mares-Nasarre, P., Gómez-Martín, M.E., Medina, J.R., *2020a*. Influence of mild bottom slopes on the overtopping flow over mound breakwaters under depth-limited breaking wave conditions. J. Mar. Sci. Eng. 8. https://doi.org/10.3390/JMSE8010003

Mares-Nasarre, P., Molines, J., Gómez-Martín, M.E., Medina, J.R., *2020b*. Individual wave overtopping volumes on mound breakwaters in breaking wave conditions and gentle sea bottoms. Coast. Eng. 159, 103703. https://doi.org/10.1016/j.coastaleng.2020.103703

Melby, J.A., *1999*. Damage progression on Rubble Mound Breakwaters. Vicksburg, MS, USA. Also Ph.D. Thesis, University of Delaware, Newark, DE, USA.

Molines, J., Herrera, M.P., Medina, J.R., *2018*. Estimations of wave forces on crown walls based on wave overtopping rates. Coast. Eng. 132, 50–62. https://doi.org/10.1016/j.coastaleng.2017.11.004

Molines, J., Medina, J.R., *2016*. Explicit wave-overtopping formula for mound breakwaters with crown walls using CLASH neural network-derived data. J. Waterw. Port, Coast. Ocean Eng. 142. https://doi.org/10.1061/(ASCE)WW.1943-5460.0000322

Molines, J., Medina, J.R., *2015*. Calibration of overtopping roughness factors for concrete armor units in non-breaking conditions using the CLASH database. Coast. Eng. 96, 62–70. https://doi.org/10.1016/j.coastaleng.2014.11.008

Nørgaard, J.Q.H., Lykke Andersen, T., Burcharth, H.F., *2014*. Distribution of individual wave overtopping volumes in shallow water wave conditions. Coast. Eng. 83, 15–23. https://doi.org/10.1016/j.coastaleng.2013.09.003

Sandoval, C., Bruce, T., *2017*. Wave overtopping hazard to pedestrians: video evidence from real accidents, in: Proc. Of Coasts, Marine Structures and Breakwaters 2017. Realising the Potential. Liverpool Waterfront, UK, pp. 501–512.

Schüttrumpf, H., Möller, J., Oumeraci, H., *2002*. OVERTOPPING FLOW PARAMETERS ON THE INNER SLOPE OF SEADIKES, in: Proc. 28th International Conference on Coastal Engineering. World Scientific Publishing Company, pp. 2116–2127. https://doi.org/10.1142/9789812791306_0178

Schüttrumpf, H., Van Gent, M.R.A., *2003*. Wave overtopping at seadikes, in: Coastal Structures 2003 - Proceedings of the Conference. pp. 431–443.

The MathWorks Inc., *2019*. MATLAB®.

Theil, H., *1961*. Economic forecasts and policy. North, Amsterdam (Holland).

van Bergeijk, V.M., Warmink, J.J., van Gent, M.R.A., Hulscher, S.J.M.H., *2019*. An analytical model of wave overtopping flow velocities on dike crests and landward slopes. Coast. Eng. 149, 28–38. https://doi.org/10.1016/j.coastaleng.2019.03.001

van der Meer, J.W., Hardeman, B., Steendam, G.J., Schüttrumpf, H., Verheij, H., *2010*. FLOW DEPTH AND FLOW VELOCITY AT CREST AND LANDWARD SLOPE OF A DIKE, IN THEORY AND WITH THE WAVE OVERTOPPING SIMULATOR. Coast. Eng. Proc. [SI]. https://doi.org/https://doi.org/10.9753/icce.v32.structures.10

van Gent, M.R.A., *2002*. WAVE OVERTOPPING EVENTS AT DIKES, in: Scientific, W. (Ed.), Proc. 28th International Conference on Coastal Engineering. World Scientific Publishing Company, Cardiff, UK, pp. 2203–2215. https://doi.org/10.1142/9789812791306_0185

van Gent, M.R.A., *2001*. Wave Runup on Dikes with Shallow Foreshores. J. Waterw. Port, Coastal, Ocean Eng. 127, 254–262. https://doi.org/10.1061/(ASCE)0733-950X(2001)127:5(254)

van Gent, M.R.A., *1999*. Physical model investigations on coastal structures with shallow foreshores. 2D model tests with single and double-peaked wave energy spectra. Delft (The Netherlands).

van Gent, M.R.A., van den Boogaard, H.F.P., Pozueta, B., Medina, J.R., *2007*. Neural network modelling of wave overtopping at coastal structures. Coast. Eng. 54, 586–593. https://doi.org/10.1016/j.coastaleng.2006.12.001

Verhagen, H.J., van Vledder, G., Arab, S.E., *2008*. A practical method for design of coastal structures in shallow water, in: Proc. 31st International Conference on Coastal Engineering. World Scientific Publishing Company, pp. 2912–2922.

https://doi.org/https://doi.org/10.1142/9789814277426_0241